Elucidation of blood-brain barrier disruption mechanism by peripheral inflammation

Yoon, Sung-Hyun

Department of Medical Science

Graduate School

Yonsei University

Elucidation of blood-brain barrier disruption mechanism by peripheral inflammation

Advisor Yu, Je-Wook

A Dissertation Submitted

to the Department of Medical Science
and the Committee on Graduate School

of Yonsei University in Partial Fulfillment of the

Requirements for the Degree of

Doctor of Philosophy in Medical Science

Yoon, Sung-Hyun

June 2025

Elucidation of blood-brain barrier disruption mechanism by peripheral inflammation

This Certifies that the Dissertation of Yoon, Sung-Hyun is Approved

Committee Chair	Kim, Chul Hoon
Committee Member	Yu, Je-Wook
Committee Member	Kim, Eosu
Committee Member	Hyun, Young-Min
Committee Member	Lee, June-Yong

Department of Medical Science
Graduate School
Yonsei University
June 2025

ACKNOWLEDGEMENTS

First and foremost, I would like to express my deepest appreciation to my advisor, professor Je-Wook Yu, for his unwavering support, invaluable guidance, and continuous encouragement throughout my Ph.D. His mentorship has shaped not only my research but also my growth as an independent scientist. I feel truly fortunate to have been a part of such an inspiring lab environment.

I would also like to extend my gratitude to all my lab members, past and present. Their constant support and insightful feedback have made this journey both enriching and enjoyable. I am sincerely grateful for the collaborative spirit and the many shared moments of learning and growth.

I am especially grateful to the members of my thesis committee for their time, guidance, and valuable feedback throughout my Ph.D. course. Professor Chul Hoon Kim provided thoughtful insights that continually pushed me to think critically and approach problems with a broader and perspective. Professor Eosu Kim offered both technical expertise and warm encouragement, which were particularly meaningful when navigating complex challenges. Professor Young-Min Hyun consistently provided constructive suggestions that helped clarify my ideas and strengthen my scientific arguments. Professor June-Yong Lee offered kind support, practical advice, and stimulating discussions that gave me confidence and motivation.

I would like to express my deepest gratitude to my family for their warm support and encouragement throughout these long academic years. Their trust in me have been the foundation on which I could stand, especially during times of doubt and difficulty. With this gratitude in my heart, I will do my best to become a more diligent and accomplished researcher, worthy of the trust and support that have given me.

TABLE OF CONTENTS

LIST OF FIGURES

LIST OF TABLES

ABSTRACT

Elucidation of blood-brain barrier disruption mechanism by peripheral inflammation

The blood-brain barrier (BBB) plays crucial roles in maintaining brain homeostasis by protecting it from peripheral toxins and inflammation. BBB disruption is a key factor that drives neuropathological conditions by enhancing neuroinflammation, yet the biological processes involved in its breakdown under physiological conditions remain poorly understood. In this study, we elucidate the involvement of the NLRP3 inflammasome in peripheral inflammation-induced BBB disruption. Repeated lipopolysaccharide (LPS) administration led to an NLRP3-dependent impairment of BBB integrity and an increase in myeloid cell infiltration into the brain. Using a mouse model with cell-specific hyperactivation of NLRP3, we demonstrate that microglial NLRP3 inflammasome activation plays a pivotal role in exacerbating peripheral inflammation-induced BBB disruption. Consistently, NLRP3 and microglial gasdermin D (GSDMD) deficiencies attenuated LPS-induced BBB breakdown, suggesting importance of microglial NLRP3-GSDMD axis in BBB disruption. Interestingly, IL-1β was not required for NLRP3-GSDMD-mediated BBB disruption. Instead, the microglial NLRP3-GSDMD axis results in the release of GDF-15 that subsequently promotes the production of CXCL chemokines in the brain, thus facilitating the recruitment of matrix metalloproteinases (MMPs)-expressing neutrophils to the brain parenchyma. Collectively, our findings highlight the critical role of microglial NLRP3-driven chemokine production which critically promotes the BBB impairment, thus suggesting potential therapeutic targets to alleviate neuroinflammation.

Key words: Blood-brain barrier, NLRP3 inflammasome, Microglial NLRP3-GSDMD axis, peripheral inflammation

1. Introduction

The brain serves as the control center of the body, essential for nearly every function. With its complex network of neurons, the brain coordinates movement, emotions, cognitions, and all fundamental physiological functions. The brain is supported by abundant glial cells to ensure the proper neuronal function. These cells help maintain the brain's homeostasis and protect it from external threats, making it a so-called "immune-privileged" organ. One of the key factors contributing to this unique immunological property is the presence of the blood-brain barrier (BBB). The BBB is a highly specialized vascular structure that protects the central nervous system (CNS) by restricting the entry of circulating immune cells and potentially harmful substances, while allowing the selective passage of specific essential nutrients and ions necessary for brain homeostasis[1]. The proper functioning of the BBB is critical for maintaining CNS homeostasis.

The structural integrity of the BBB is governed by a dynamic interplay between endothelial cells, pericytes, and astrocytes, which cooperatively regulate barrier permeability[2]. Endothelial cells form a continuous monolayer with tight junction proteins that reinforce the barrier function. The tight junctions formed by brain endothelial cells are significantly more robust than those in other organs, contributing to the highly selective permeability of the BBB[3]. The limited expression of adhesion molecules on BBB endothelial cells serves to restrict immune cell entry into the CNS[4]. However, during neuroinflammation, the expression of these molecules is upregulated, facilitating the recruitment and transmigration of immune cells[5]. In addition to regulating immune cell infiltration, BBB endothelial cells actively mediate the transport of essential nutrients, metabolites, and ions via specific transporters and receptor-mediated mechanisms[6]. Through these transport processes and strict barrier properties, the BBB contributes significantly to CNS homeostasis through its regulation of the brain's microenvironment. Pericytes play a crucial role in the maintenance of the BBB by regulating tight junction integrity in endothelial cells, suppressing transcytosis, and promoting vascular stability. They also engage in bidirectional signaling with endothelial cells and glial cells, thereby contributing to CNS homeostasis and modulating inflammatory responses[7,8]. Astrocytes contribute to the maintenance of BBB integrity by releasing various soluble factors that reinforce endothelial barrier properties. Their perivascular end-feet regulates ionic and metabolic homeostasis and plays a key role in neurovascular coupling[9]. Under

pathological conditions, reactive astrocytes can influence BBB permeability and neuroinflammatory processes[10,11].

Disruption of BBB integrity is a hallmark feature of various neuropathological conditions, including ischemic stroke, neurodegenerative and neurological diseases such as Alzheimer's disease (AD) and Parkinson's disease (PD), epilepsy, and brain tumors[12-14]. BBB breakdown is associated with various detrimental factors, including oxidative stress, pro-inflammatory cytokines, aberrant protein aggregation, and pathogenic infiltration, which collectively exacerbate neuroinflammation and disease progression[15,16]. For example, several magnetic resonance imaging (MRI)-based neuroimaging studies have revealed that the BBB disruption in the hippocampus is observed before hippocampal atrophy, which is typically implicated in early AD patients[17,18]. These studies suggest the possibility that BBB breakdown might be an initiating factor that critically drives neurodegeneration. Damages in BBB also cause cerebral microbleeds in the brain, which is positively correlated with amyloid deposition in the brain in patients with mild cognitive impairment and AD, as determined by 18F-florbetapir positron emission tomography (PET)[19,20]. The post-mortem fixed brain tissues of PD patients demonstrated a significant loss in BBB integrity and subsequent extravasation of serum proteins such as albumin and fibrinogen in the brain, and infiltrations of lymphocytes were also observed[21,22]. In addition, brain MRI imaging of patients with temporal lobe epilepsy exhibits BBB leakage and its negative correlation with expressions of tight junction molecule Claudin 5 in the hippocampus[23]. In line with this, conditional knockdown of Claudin 5 expression in the hippocampus aggravates epilepsy pathogenesis in mice, collectively suggesting a correlation between BBB stabilization and epilepsy disease progression[24]. Despite mounting evidence implicating BBB dysfunction in neurological disorders, the precise molecular mechanisms governing BBB permeability under pathological conditions remain poorly understood.

Despite its tightly regulated structure, accumulating evidence suggests that the BBB is highly susceptible to various external challenges, including systemic inflammation, microbial toxins, and metabolic disturbances[25-27]. Among these, systemic inflammation is a particularly potent disruptor, as it triggers a cascade of immunological and physiological events that act on the neurovascular unit. Recent studies have reported that systemic inflammatory conditions such as COVID-19[28-30], systemic lupus erythematosus (SLE)[31], and sepsis[32] are associated with compromised BBB integrity, characterized by increased vascular permeability and neurovascular dysfunction. Although the exact mechanisms underlying these clinical observations remain unclear, studies using experimental

models of systemic inflammation have identified several contributing factors, including the release of circulating inflammatory mediators, enhanced leukocyte activation and recruitment, and hemodynamic alterations[26,33]. The BBB's reaction to systemic inflammatory stimuli can be categorized into a spectrum of changes, ranging from altered endothelial signaling and increased cellular trafficking to elevated solute permeability and structural damage involving endothelial cells, the basement membrane, pericytes, and astrocytic end-feet[25,34]. This progressive disruption underscores the dynamic interplay between peripheral immune activation and central nervous system vulnerability[35,36].

Various studies have reported BBB alterations under systemic inflammatory conditions[33,37-39]. Given the brain's status as an immune-privileged organ, many early investigations highlighted structural changes in endothelial cells following peripheral immune activation. There are several characteristic mechanisms by which peripheral inflammation leads to BBB dysfunction, each involving distinct yet interrelated molecular and cellular responses. Peripheral inflammation exerts multifaceted effects on the BBB, altering both its structural integrity and functional properties. These effects can be broadly categorized into five major mechanisms[40]. First, tight junction proteins including claudin-5, occludin, junctional adhesion molecules (JAMs), and zonula occludens (ZO)-1 are particularly sensitive to inflammatory signals. Exposure to cytokines such as IL-1β, TNF-α, IL-17, and IL-6 often leads to their downregulation, redistribution, or degradation, thereby weakening the tight junction of endothelial cells and thus increasing BBB permeability[41]. Second, endothelial cells themselves undergo a range of stress responses under inflammatory conditions. These include apoptosis, altered expression of transporters, and increased expression of adhesion molecules such as VCAM-1 and ICAM-1, which promote leukocyte adhesion and transendothelial migration into the parenchymal region[34]. Third, glial cells, especially astrocytes and microglia, modulate BBB function upon peripheral inflammation. Astrocyte and pericyte-derived factors such as vascular endothelial growth factor (VEGF) can reduce tight junction protein expression in neighboring endothelial cells, while activated microglia releases proinflammatory mediators and reactive oxygen species that contribute to barrier disruption[42,43]. Finally, peripheral immune cells infiltrate the CNS and exacerbate BBB breakdown. T cells, B cells, neutrophils, and monocytes produce cytokines and matrix metalloproteinases (MMPs) that further compromise endothelial integrity and promote local inflammation[44].

Accumulating evidence indicates that inflammatory stimuli, such as circulating cytokines, preferentially localize to the luminal surface of brain endothelial cells, where they can directly impair endothelial function and compromise the integrity of the BBB[45-47]. As a result, studies on BBB were mostly focused on endothelial cells regardless of multicellular structure of the BBB. Several studies have demonstrated that the treatment of lipopolysaccharide or cytokine such as IL-1β, and TNFα to brain endothelial cell lines results in a substantial reduction in the expression of tight junction molecules and a robust increase in BBB permeability, indirectly suggesting that inflammation can indeed induce endothelial cell death and impair the BBB[48,49]. However, the interplay between brain-resident cells and peripheral immune components in the context of systemic inflammation-induced BBB disruption remains to be fully elucidated. Few recent studies have demonstrated that peripheral inflammation induced by intraperitoneal injections of LPS can activate microglia and trigger their migration towards BBB. These studies also demonstrate that the administration of minocycline, which inhibits microglial activity, effectively reduces BBB permeability[50]. However, the mechanisms by which microglia influence BBB integrity remain to be fully elucidated.

Microglia, the resident macrophages of the CNS, continuously surveil the brain microenvironment and serve as the primary responders to pathological insults by detecting damage-associated molecular patterns (DAMPs) and pathogen-associated molecular patterns (PAMPs) through pattern recognition receptors such as Toll-like receptors (TLRs) and Nod-like receptors (NLRs)[51]. Inflammasome is a multi-protein complex that activates caspase-1. Five receptor proteins are known as inflammasome components, including NLR family pyrin domain-containing 1, 3 (NLRP1, NLRP3) and NLR family CARD domain-containing protein 4 (NLRC4), as well as the proteins absent in melanoma 2 (AIM2) and pyrin[52,53]. Among them, NLRP3 inflammasome responds to diverse stimulus, including crystalline and particulate matter (such as MSU, silica, asbestos and alum), extracellular ATP, nigericin and several viral, bacterial, fungal and protozoan pathogens. Extracellular ATP or crystalline stimuli can cause potassium efflux and lysosomal rupture, respectively. NLRP3 inflammasome activation requires priming step that involves the transcription of pro-IL-1β and NLRP3. Subsequent to the priming step, extracellular ATP or crystalline stimulation activates NLRP3 inflammasome that assembles oligomerization of NLRP3, apoptosis-associated speck-like protein containing a caspase recruitment domain (ASC) and pro-caspase-1[54]. The assembly of the inflammasome acts as a critical regulator of innate immunity by sensing cellular

stress and triggering the activation of caspase-1, leading to the cleavage of gasdermin D (GSDMD) and the subsequent release of pro-inflammatory cytokines IL-1β and IL-18[55]. Upon activation, microglia mediate inflammatory responses through cytokine secretion, peripheral immune cells recruitment, and extensive interactions with astrocytes or neurons, thereby playing a pivotal role in driving neuroinflammation and brain disorders[56]. In line with this, the cleavage of caspase-1, IL-1β, and IL-18 were elevated in postmortem brain tissue of stroke patients, and pharmacological inhibitors of NLRP3 inflammasome components, such as MCC950 or Anakinra treatment, effectively ameliorated injuries in experimental mouse models of stroke. Moreover, in the transgenic APP/PS1 model used to study AD, the deficiency in NLRP3 indeed alleviated spatial memory impairment and significantly reduced the Aβ plaque deposition and inflammation in the hippocampus[57]. Although aberrant activation of the NLRP3 inflammasome has been associated with the development of various neuroinflammatory and neurodegenerative diseases, its direct contribution to BBB permeability regulation remains unclear.

The BBB comprises a highly specialized multicellular structure mainly made up of endothelial cells, pericytes, astrocytic end-feet, and the extracellular matrix[58]. Despite this complexity, much of the current research on BBB disruption, particularly under inflammatory conditions, has relied heavily on in vitro models using brain endothelial cells only[48,59]. While these simplified systems offer mechanistic insights into endothelial cell-specific responses, they fail to recapitulate the physiology of intricate cellular interactions and dynamic microenvironment. Therefore, to fully understand the pathophysiology of BBB dysfunction and the contribution of non-endothelial components—such as astrocytes, pericytes, and microglia—it is essential to employ in vivo models. These systems allow for the investigation of context-dependent signaling, cell-cell communication, and systemic influences that are indispensable for delineating the multifactorial mechanisms underlying BBB impairment.

In the present study, we examine the impact of peripheral inflammation on BBB integrity by examining the cellular and molecular responses of brain-resident glial cells upon systemic lipopolysaccharide (LPS) challenge in a murine model. Our findings reveal that LPS-induced systemic inflammation triggers microglial NLRP3 inflammasome activation. We demonstrate that the microglial NLRP3-GSDMD axis plays a crucial role in BBB disruption in an IL-1β or IL-18-independent manner, suggesting an alternative inflammatory mechanism governing BBB permeability under systemic inflammatory conditions. Notably, rather than vascular-derived

molecules directly compromising brain endothelial integrity, microglial activation is a necessary precursor to BBB disruption. Additionally, we identify neutrophil recruitment to the brain vasculature as a critical event following microglial NLRP3 inflammasome activation. Upon arriving at the vascular site, neutrophils release MMPs that degrade the extracellular matrix and contribute to BBB breakdown. This further underscores the importance of cellular interactions in the regulation of BBB integrity. Given that BBB integrity is tightly maintained by multiple cellular components, it can effectively resist external molecules in the absence of microglial activation and neutrophil recruitment. By delineating cellular interactions and molecular pathways contributing to BBB compromise, our study provides novel perspectives on the mechanisms underlying neurovascular dysfunction and highlights potential therapeutic targets for preserving BBB integrity in inflammatory diseases.

2. MATERIAL & METHODS

2.1. Mice

C56BL/6, *NLRP3*^{D301NneoR}, *Il-1r1*$^{-/-}$, *Gsdmd*$^{-/-}$, *Ccr2*$^{-/-}$, *CX3cr1-creERT2, Tmem119-creERT2,* and *Aldh1l1-creERT2* mice were obtained from The Jackson Laboratory and bred at Yonsei University College of Medicine. All mice were maintained under specific pathogen-free conditions. Male and female mice at the age of 8 – 12 weeks were used for the experiments. Protocols for the animal experiments were approved by and were performed in accordance with the Institutional Ethical Committee of Yonsei University College of Medicine. *NLRP3*^{D301NneoR} mice were bred with *CX3cr1-creERT, Tmem119-creERT,* or *Aldh1l1-cre/ERT2* to generate transgenic mice that express NLRP3 (D301N) mutant form specifically in myeloid cells, microglia, and astrocytes, respectively. To induce Cre recombinase expression, tamoxifen was given intraperitoneally at 75 mg/kg once per day for fice successive days. All experiments were done after having 1 week of resting phase following the last tamoxifen injection to avoid any tamoxifen-dependent side effects in these mice[60,61].

2.2. Peripheral inflammation-induced BBB disruption model *in vivo*

To establish a mouse model of peripheral inflammation-induced BBB disruption, mice were intraperitoneally administered LPS (sigma, L3012) at dose of 0.8 mg/kg, either one or two times with a 24-hour intervals[62]. A cytokine cocktail consisting of IL-1β at a dose of 10 μg/kg body weight, IL-6 at 35 μg/kg body weight, and TNF-α at35 μg/kg body weight was injected into mice via the tail vein three times at 6 h or 18 h intervals[60]. Serum cytokine levels were measured to determine the peripheral inflammation, and BBB permeability assays were employed to evaluate BBB disruption in this model.

2.3. *In vivo* experimental procedure

For NLRP3 inhibitor experiments, mice were given an intraperitoneal injection of MCC950 (Sigma, PZ0280) 30 minutes prior to the LPS injection at a dose of 10 mg/kg. Anakinra (Prospec, cyt-203), the IL-1 receptor antagonist, was administered at 10 mg/kg via intraperitoneal injection,

30 minutes prior to the LPS injection[63]. Ilomastat, the pan-MMP inhibitor, was injected at a dose of 50 mg/kg 6 hours after the final LPS injection via intraperitoneal injection. For GDF-15 administration, mice received a retro-orbital injection of GDF-15 at a dose of 2 μg per mouse, and the animals were sacrificed 6 hours post-injection for subsequent analysis[60].

2.4. BBB permeability assay

To evaluate BBB permeability, the extravasation of tail vein-injected Evans blue dye or sodium fluorescein in brain parenchyma was quantified. Evans blue (Sigma, E2129) or sodium fluorescein was intravenously injected at a dose of 0.2 mg/kg or 11 mg/kg, respectively, via the tail vein[60,61,64]. After 1 hour, following deep anesthesia, mice were perfused through the heart with cold PBS. Brain tissues were collected after removing the skull and the meninges. The weight of the brain tissue was measured and then homogenized in saline by means of a dounce grinder. The Evans blue was extracted in the supernatants using tricholoracetic acid (Sigma, T6399) precipitation method. Then, the Evans blue fluorescence was measured using Varioskan Flash 3001 microplate fluorometer (Thermo Fisher) at 620 nm excitation and 680 nm emission[61]. For sodium fluorescein quantification, brain tissues were homogenized in Triton X-100 (1%) in PBS solution, and the fluorescence in the resulting supernatant was measured at 492 nm excitation/ 525 nm emission[60].

2.5. Single cell suspension preparation

Mice were transcardially perfused with ice-cold PBS under deep isoflurane anesthesia. Brain tissue was carefully isolated and homogenized at RPMI-1640 supplemented with collagenase IV (Sigma, C5138) and DNase I (Biolabs M303s) using dounce grinder. Olfactory bulbs, brainstems, and meninges were excluded from all analysis. The tissue homogenates were subjected to incubation at 37°C for 40 minutes for dissociation, and then further filtered using sterile 70 micron cell strainers to acquire single cell suspension. The cells were subjected to 30% Percoll (Sigma, P1644) diluted in 1X HBSS solution for myelin debris removal and were centrifuged at 700g for 25 minutes at 20°C with no acceleration or deceleration brake to avoid disrupting the gradient. After centrifugation, the myelin and debris present in the top and interphase layers were aspirated, and the remaining cell pellet was resuspended in PBS containing 5% fetal bovine serum (FBS).

All steps were done at 4°C unless otherwise mentioned to ensure the cell viability and purity[60,61].

To prepare single cells for scRNA-sequencing, the brain tissues collected from mice were enzymatically dissociated using the Adult Brain Dissociation kit (Miltenyi Biotec, 130-107-677) following the supplier's guidelines. The debris removal solution was used to eliminate myelin and debris, and red blood cells were lysed with RBC remonal reagent included in the kit. For preparation of each experimental group (PBS, LPS x1, LPS x2), brain hemispheres from two males and one female were pooled into a single replicate[60].

2.6. Flow cytometry

Brain cells were resuspended in FACS staining buffer, consisting of 5% FBS diluted in PBS, and subsequently incubated with fluorochrome-conjugated antibodies targeting CD45, CD11b, Ly6G, and Ly6C (Biolegend; 103116, Invitrogen; 12-0112-82, Invitrogen; 17-9668-82, Invitrogen; 53-5932-82, respectively). To exclude dead cells, samples were counterstained with DAPI (Invitrogen, D1306). Flow cytometry analysis was performed using FACS Verse (BD Biosciences), and the resulting data were analyzed using Flowjo software (TreeStar)[60,61].

2.7. Immunohistochemistry

Under deep anesthesia using isoflurane, transcardial perfusion of mice was performed using cold PBS, followed by 4% paraformaldehyde (PFA) for tissue fixation. The whole brain tissue was carefully collected and further fixed at 4% PFA overnight at 4°C. Then, the fixed brain tissue was transferred to 30% sucrose prepared in PBS and incubated at 4°C for approximately 48 hours for complete dehydration. After the tissue sank to the bottom, it is embedded in Optimal Cutting Temperature (OCT) compound to preserve the tissue in a fresh frozen block, which is then cryosectioned into fresh frozen slices using a Leica CM1860 cryostat at -20°C. The brain is coronally sectioned into 30 μm thick slices and transferred onto charged glass slides.

For intracellular staining, the slides were incubated in 0.3% Triton-X (in PBS) for 30 minutes for permeabilization. After washing the slides using PBS supplemented with Tween 20 (PBST), the slides were then subjected to blocking solution (4% BSA in PBS) for 1 hour at room temperature (RT). Then, the primary antibodies, anti-GFAP (Invitrogen, PA1-10004, 1:2000) and anti-Iba1 (Wako, 019-19741, 1:500), diluted in 1% BSA, were applied to the slides and incubated

overnight at 4°C. The slides were washed 5-6 times using PBST, and subsequently incubated with secondary antibodies for 3 hours at RT. To visualize nuclei, the slides were stained with DAPI and mounted with a mounting solution (Invitrogen, P36934) for tissue perseverance. Then, the slides were carefully covered with coverslip. Using the LSM980 confocal microscope (Carl Zeiss), 20 images were acquired in Z-stack format at 1 μm intervals and analyzed with Zen Blue software.

2.8. *Ex vivo* active caspase-1 detection

To detect active caspase-1 activity in brain and peripheral organs, mice were given intravenous injection of the caspase-1-specific probe (100 μg/ mouse) via the tail vein. Following a 1-hour period, mice were anesthetized with isoflurane, followed by transcardial perfusion with cold PBS. Brain, lung, and spleen were subsequently harvested for *ex vivo* imaging with an IVIS spectrum In Vivo imaging system (PerkinElmer). The presence of caspase-1 was required for Cy5.5 fluorescence to be detected[65].

2.9. Neutrophil depletion

Mice were administered with intraperitoneal injections of 50 μg of anti-mouse Ly6G (Bio X Cell, BE0075-1) antibody targeting mouse neutrophils or isotype control IgG (Bio X Cell, BE0089) antibody 1 hour before the first LPS injection only. The populations of neutrophils in the blood samples were analyzed using flow cytometry to confirm the neutrophil depletion (data not shown).

2.10. Immunoblot analysis

The brain tissues were lysed in TEN buffer consist of 10 mM Tris-Cl (pH 7.4), 2 mM EDTA, 150 mM NaCl, and protease inhibitors. The soluble protein lysates were separated by sodium dodecyl sulfate-polyacrylamide gel electrophoresis (SDS-PAGE) and subsequently transferred onto polyvinylidene difluoride (PVDF) membranes. The membranes were then incubated with appropriate primary antibodies followed by horseradish peroxidase (HRP)-conjugated secondary antibodies[53]. All blots are representative of at least three independent experiments.

2.11. Enzyme-linked immunosorbent assay (ELISA)

Whole blood was collected from the orbital sinus of mice using capillary tubes and stored at 4°C for 1-2 hours to allow clot formation. Then, the samples were centrifuged at 2000g for 17 minutes at 4°C, in which the serum is obtained from the supernatant layer. The serum samples were diluted for ELISA assay. Brain tissues were homogenized in TEN buffer supplemented with protease inhibitors using a Dounce homogenizer to prepare tissue lysates. The resulting homogenates were centrifuged, and the supernatants were collected for protein quantification using Bradford assay. The concentrations of IL-1β, IL-6, IL-18, CXCL1, CXCL2, and MMP9 were determined by ELISA using DuoSets kit (R&D systems), following the manufacturer's instructions.

2.12. Quantitative real-time PCR

Total RNA was extracted from brain tissues and cultured cells using TRIzol reagent (Invitrogen). Reverse transcription was carried out with a primer mix (Takara) to synthesize complementary DNA (cDNA). Quantitative real-time PCR was performed using SYBR Green reagents (Takara, ABclonal) to assess gene expression levels, with *Rn18s* serving as internal control.

2.13. Cell cultures

Primary mixed glial culture was obtained from whole brains of mouse pup on postnatal days 0-3. Brains were placed in ice-cold 2X HBSS, and the meninges and cerebellum were carefully removed. The tissues were then dissociated using a fire-polished Pasteur pipette, and the resulting cell suspension was passed through a 70 μm cell strainer to remove debris and aggregates. The cells were then cultured at Dulbecco's Modified Eagle Medium/Nutrient Mixture F-12 (DMEM/F12) supplemented with 10% FBS and 1% penicillin/streptomycin (p/s) into poly-D-lysin-coated T75 flasks for 14 days. After 7 days when a confluent mixed glial layer is formed, medium was changed every 2-3 days. For microglia enrichment, the flask was shaken at 180 rpm for 4 hours, so that the microglia were detached. The media were collected and plated onto well plates for experiments.

For bone marrow-derived macrophages (BMDMs) culture, the femur of adult mice was

isolated and flushed using 5 ml syringes with cold PBS. The bone marrow cells were obtained and filtered through 70 μm strainer and were cultured in L929-conditioned DMEM supplemented with 10% FBS and 1% p/s for 5 days for BMDM differentiations[66].

2.14. Secretome analysis by mass spectrometry

The primary microglia cultures were plated onto 6 well plates and were treated either with LPS (0.25 μg/ml, 3h), followed by ATP (2.5 mM, 20 min), or with ATP alone. The cell-free supernatants from WT and *Gsdmd*-deficient microglia were collected and subjected to mass spectrometry analysis. For protein digestion, 140 μl of each supernatant was combined with 60 μl of 100 mM triethylammonium bicarbonate (TEAB) buffer at pH 8.5. The sample were reduced with 200 mM Tris 2-carboxyethyl phosphine (TCEP) at 55°C for 1 hour and subsequently alkylated with 375 mM iodoacetamide (IAA) for 30 minutes in the dark. Proteins were precipitated with acetone, then reconstituted in 100 mM TEAB buffer and enzymatically digested with trypsin at 37°C for 16 hours. The resulting peptides were labeled using the TMT 10plex™ isobaric tagging reagent (Thermo Fisher Scientific) according to the manufacturer's instructions for relative quantification. After vacuum concentration, the peptides were desalted using spin columns (Thermo Fisher Scientific), dried again, and resuspended in 0.1% formic acid. Mass spectrometry analysis was carried out with a Dionex Ultimate 3000 RSLC nano-HPLC system coupled to an Orbitrap Q Exactive mass spectrometer (Thermo Fisher Scientific). Protein quantification and normalization were performed using Proteome Discoverer 2.3 software (Thermo Fisher Scientific).

2.15. Single-cell transcriptomic analysis

Single-cell libraries were constructed using the Chromium Controller following the 10X Chromium Next GEM Single Cell 3' v3.1 protocol (CG000315). Initially, single-cell suspensions were prepared by diluting cells in nuclease-free water to achieve a target cell number of around 10,000 per sample. Equal volumes of the suspensions were transferred onto the Chromium Next GEM chip at equal cell concentrations, enabling capture, unique barcoding, and reverse transcription of RNA from individual cells. The resulting complementary DNA was subjected to purification and amplification via polymerase chain reaction (PCR), producing the final library.

Library quantification was performed using qPCR following the qPCR Quantification Protocol Guide, while library quality was evaluated using an Agilent 4200 Technologies TapeStation system. Sequencing of the prepared libraries was performed on the Illumina HiSeq platform following the manufacturer's recommended read length parameters.

For single-cell transcriptomic analysis, raw sequencing reads were processed using Cell Ranger software version 7.1.0 (10x Genomics). Initially, BCL files obtained from the Illumina platform were demultiplexed into FASTQ format using 'cellranger mkfastq.' These FASTQ files were subsequently analyzed with 'cellranger count,' which involved alignment to the mm10-2020-A mouse reference genome, quantification of gene expression based on unique molecular identifiers (UMIs), and identification of cell clusters. Differentially expressed genes (DEGs) were identified through statistical analysis. To integrate data from multiple independent samples, the 'cellranger aggr' function was utilized. Downstream bioinformatics analyses were carried out using the Scanpy package in Python. Principa component analysis (PCA) served as the basis for cell clustering and UMAP visualization. DEGs between experimental and control groups were identified using the Wilcoxon rank-sum test implemented through the 'FindMarkers' function in Scanpy, with multiple testing corrections applied using adjusted p-values and Bonferroni adjustments to control the false discovery rate (FDR). Functional enrichment and pathway analyses of the significantly regulated genes were performed using g:Profiler (https://biit.cs.ut.ee/gprofiler/).

2.16. Image processing and analysis

The Z-stack images were merged and processed using "orthogonal projections" methods in Zen blue software. Cell number quantification and measurement of mean fluorescence intensity (MFI) were conducted using ImageJ software. All parameters were uniformly applied across both control and experimental groups. The cell numbers and MFI of astrocytes and microglia-identified as $GFAP^+$ and $Iba1^+$ cells, respectively-were quantified and subsequently normalized to the total number of $DAPI^+$ nuclei.

2.17. Statistical analysis

DATA are expressed as the mean ± standard error of the mean (SEM). Statistical significance

was assessed using an unpaired two-tailed Student's t-test, one-way ANOVA followed by Dunnett's post hoc correction, or two-way ANOVA with Bonferroni post hoc correction, as appropriate. A P-value of ≤ 0.05 was considered statistically significant. GraphPad Prism software version 8.0 was utilized for performing all statistical analyses.

Table 1. Primer sequence for PCR

Gene	Primer sequence
Mouse *Cxcl1*	Forward: 5′- GCT GGG ATT CAC CTC AAG AA -3′ Reverse: 5′- TGG GGA CAC CTT TTA GCA TC -3′
Mouse *Cxcl2*	Forward: 5′- GTT TCT GGG GAG AGG GTG GAG -3’ Reverse: 5′- TGT TCT ACT CTC CTC GGT GC -3’
Mouse *Cxcl3*	Forward: 5′- AGA CCA TCC AGA GCT TGA CG -3′ Reverse: 5′- GGA CTT GCC GCT CTT CAG TA -3′
Mouse *Cxcl5*	Forward: 5′- TTC CTC AGT CAT AGC CGC AA -3′ Reverse: 5′- TGG ATC CAG ACA GAC CTC CT -3′
Mouse *Ccl2*	Forward: 5′- AGG TGT CCC AAA GAA GCT GT -3′ Reverse: 5′- ACA GAA GTG CTT GAG GTG GT -3′
Mouse *Ccl11*	Forward: 5′- GCC ATA GTC TTC AAG ACC AAG CTT -3′ Reverse: 5′- TGG CAT CCT GGA CCC ACT T -3′
Mouse *Ccl13*	Forward: 5′- CAA ACT GGG CAA GGA GAT CTG -3′ Reverse: 5′- GGC CCA GGT GTT TCA TAT AAT TCT -3′
Mouse *Cx3cr1*	Forward: 5′- GCA GAT CCC CAG AAA CTG AG -3′ Reverse: 5′- GGC ACC AGG ACG TAT GAG TT -3′
Mouse *Gdf15*	Forward: 5′- GAC ATC ACT AGG CCC CTG AA -3′ Reverse: 5′- TTC AAG AGT TGC CTG CAC AG -3′
Mouse *Mmp8*	Forward: 5′- TCG CCT GAA GAC ACT TCC AT -3′ Reverse: 5′- GCG CTG CAT CTC TTT AAG CT -3′
Mouse *Mmp9*	Forward: 5′- CTT CTG GCG TGT GAG TTT CCA -3′ Reverse: 5′- ACT GCA CGG TTG AAG CAA AGA -3′
Mouse *Rn18s*	Forward: 5′- CGC GGT TCT ATT TTG TTG GT -3′ Reverse: 5′- AGT CGG CAT CGT TTA TGG TC -3′

3. Results

3.1. Peripheral LPS stimulation induces neuroinflammation and BBB disruption

To explore the impact of peripheral inflammation on BBB integrity and immune responses, we first adopted lipopolysaccharide (LPS)-administration method to induce peripheral inflammation in mice[62]. Considering that LPS is a potent endotoxin capable of inducing robust inflammation, we selected a sublethal LPS dose of 0.8 mg/kg to minimize its extreme side effects on brain environment. Mice received intraperitoneal injections of LPS either once or twice at 24-hour intervals, and the BBB permeability was examined 6 hours after the final LPS injections (Fig. 1 a). Evans blue dye was intravenously injected into mice 5 hours after the last LPS injection. We observed a significant deposition of the Evans blue dye into the peripheral organs such as spleen and lung following both single and double LPS injections (Fig. 1 b). By contrast, BBB remained intact upon a single LPS injection, while a robust Evans blue dye extravasation into the brain was observed following two repeated LPS injections (Fig. 1 b, c). Likewise, we detected a marked increase in NaF leakage in the brain upon repeated LPS injections, indicating the loss in BBB integrity upon peripheral inflammation (Fig. 1 d).

Next, to further evaluate the brain's inflammatory status following peripheral inflammation, we measured proinflammatory cytokine levels in the brain (Fig. 2a). Repeated LPS injection led to increased concentrations of IL-6 and IL-1β, indicating both BBB disruption and the initiation of inflammatory responses within the brain (Fig. 2 b, c). Western blot analysis further demonstrated a marked elevation in the processing of pro-IL-1β to its bioactive form in the brain upon repeated LPS injections (Fig. 2 d). Since IL-1β cleavage is normally associated with NLRP3 inflammasome activation[67], an increase in NLRP3 levels was also detected following LPS injections, along with the IL-1β cleavage (Fig. 2 d). Consistent with our previous data showing the BBB remains unaffected upon a single LPS injection (Fig. 1), proinflammatory cytokines were also not observed following a single LPS injection (Fig. 2 b, c, d). Meanwhile, we did not observe any changes in brain IL-18 levels, another cytokine associated with NLRP3 inflammasome activation (Fig. 2 e).

To further examine the impact of peripheral inflammation on the brain, we analyzed immune cell populations using flow cytometry (Fig. 3 a, b). In addition to the observed BBB disruption upon repeated LPS injections, we observed marked increase in $CD45^{+}$ overall immune cells and $CD45^{hi}CD11b^{hi}$ infiltrating myeloid populations within the brain, while the population of brain-resident microglial remained unaffected (Fig. 3 c, d, e). Among the infiltrating cells, the majority were neutrophils ($Ly6G^{+}$, $Ly6C^{int}$), with a smaller proportion being monocytes ($Ly6G^{-}$, $Ly6C^{+}$) (Fig. 3 f, g). Since the significant BBB disruption was observed following peripheral inflammation with twice-daily LPS injections, this protocol was used for the rest of the study to unravel the mechanism unless otherwise mentioned.

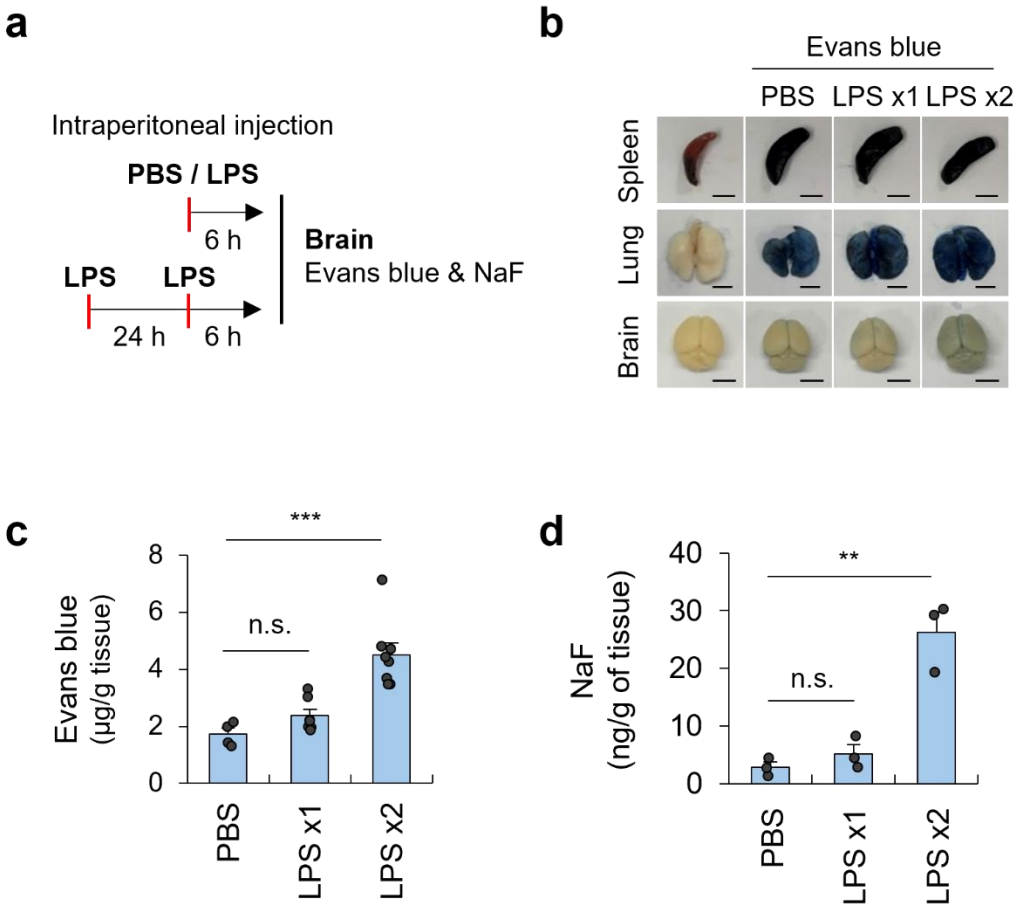

Fig 1. Repeated intraperitoneal LPS injections induce BBB disruption. (a) Schematic of the experimental design for LPS-induced brain inflammation in wild-type (WT) mice. Mice administered either a single or two intraperitoneal injections of LPS (0.8 mg/kg; 24-hour interval). BBB permeability was assessed 6 hours after the final LPS injection. Evans blue or sodium fluorescein (NaF) was administered via tail vein 1 hour prior to anesthesia. All animals were perfused to eliminate contamination of intravascular Evans blue dye. (b) Representative organ images from the Evans blue assay in mice injected with PBS or LPS, collected 6 hours after the final injection. “LPS x1” indicates a single LPS injection, and “LPS x2” indicates two LPS injections in an interval of 24 h. Scale bars = 0.5 cm. (c) Quantification of Evans blue deposition per gram of brain tissue from (b). (n = 4 (PBS), 7 (LPS x1), 8 (LPS x2)). (d) Quantification of NaF leakage per

gram of brain tissue from mice at 6 hours post- PBS or LPS injections (n = 3 per group). Differences among groups were performed through one-way ANOVA, subsequently analyzed using Dunnett's post hoc analysis, asterisk used to denote statistically significant differences. Data is expressed as means ± SEM (c, d). $^{**}P < 0.01$, $^{***}P < 0.001$, n.s. not significant.

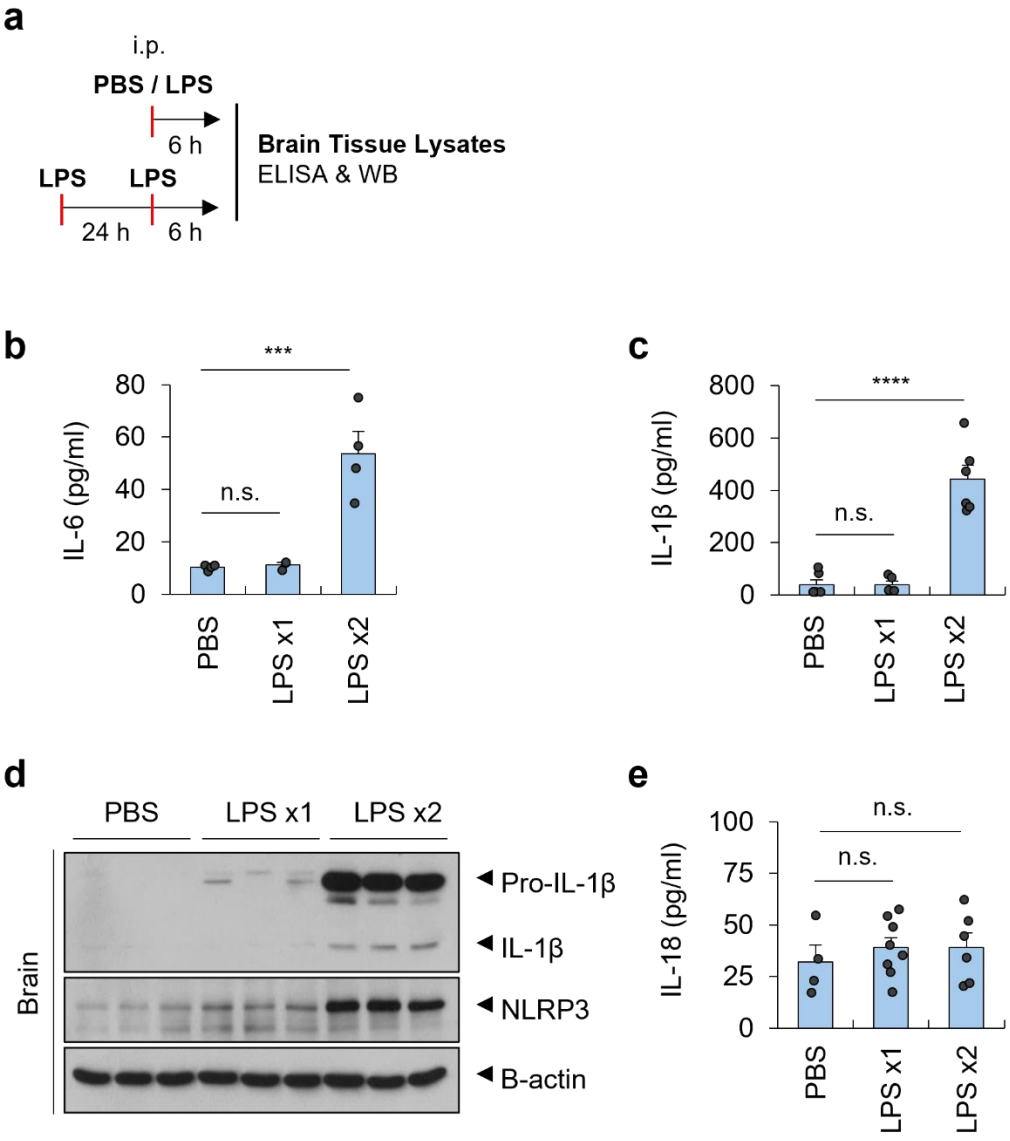

Fig 2. Repeated intraperitoneal LPS injections induce brain inflammation. (a) Schematic of the experimental design for LPS-induced brain inflammation in WT mice. Mice administered either a single or two intraperitoneal injections of LPS (0.8 mg/kg; 24-hour interval). Brain Tissue lysates were collected for ELISA and Immunoblot analysis to assess brain inflammation in response to

peripheral inflammation. (b, c) Quantitative analysis of IL-6 (b) and IL-1β (c) protein concentrations in the brain lysates (6 hours after the final injection). “LPS x1” indicates a single LPS injection, and “LPS x2” indicates two LPS injections in an interval of 24 h. (n = 4 or 6 (PBS), 3 or 5 (LPS x1), 4 or 6 (LPS x2)). (d) Immunoblot analysis of brain lysates from WT mice treated with PBS or LPS, detecting pro-IL-1β, mature IL-1β, NLRP3, and β-actin. (e) Quantitative measurement of IL-18 protein level in the lysates of mouse brain using ELISA. (n = 4 (PBS), 8 (LPS x1), 6 (LPS x2)). Differences among groups were performed through one-way ANOVA, subsequently analyzed using Dunnett’s post hoc analysis, asterisk used to denote statistically significant differences. Results are shown as means ± SEM (b, c, e). ***$P < 0.001$, ****$P < 0.0001$, n.s. not significant.

a

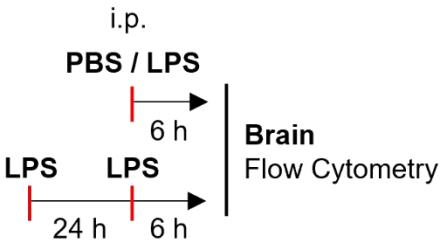

b

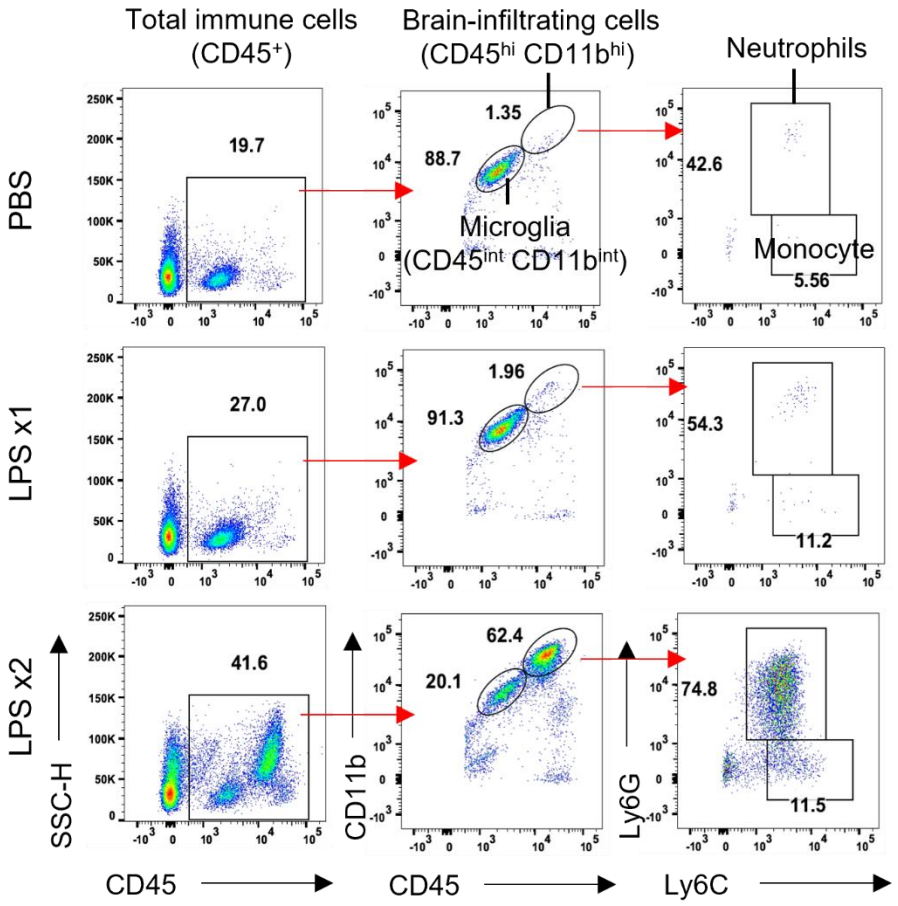

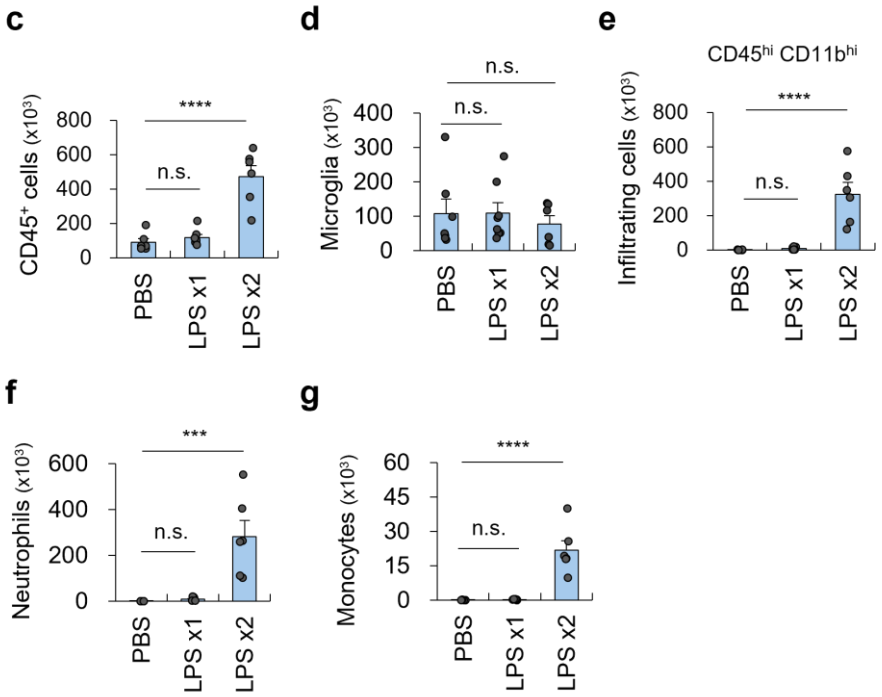

Fig 3. Repeated intraperitoneal LPS injections lead to robust myeloid cell infiltrations into the brain. (a) Schematic representation of protocol for inducing brain inflammation by LPS administration in WT mice. Mice administered either a single or two intraperitoneal injections of LPS (0.8 mg/kg; 24-hour interval). Fresh brain tissues were collected for flow cytometry analysis. (b) Flow cytometry gating strategy illustrating the identification of total immune cells ($CD45^{+}$), microglia ($CD45^{int}$, $CD11b^{int}$), infiltrating myeloid populations ($CD45^{hi}$, $CD11b^{hi}$), neutrophils ($CD45^{hi}$, $CD11b^{hi}$, $Ly6C^{int}$, $Ly6G^{+}$), and monocytes ($CD45^{hi}$, $CD11b^{hi}$, $Ly6C^{+}$, $Ly6G^{-}$) in the brain samples from PBS, LPS x1, and LPS x2 injected groups. "LPS x1" indicates a single LPS injection, and "LPS x2" indicates two LPS injections in an interval of 24 h. (c, d, e, f, g) Flow cytometry quantification of immune populations in the brain, including total immune cells (c), microglia (d), infiltrating cells (e), neutrophils (f), and monocytes (g), following PBS- or LPS-administration (6 h post last injection). (n = 6 (PBS), 7 (LPS x1), 6 (LPS x2)). Differences among groups were performed through one-way ANOVA, subsequently analyzed using Dunnett's post hoc analysis, asterisk used to denote statistically significant differences. Results are shown as means ± SEM (c, d, e, f, g). ***$P < 0.001$, ****$P < 0.0001$, n.s. not significant.

3.2. Brain inflammation occurs at an earlier time point than BBB disruption following peripheral inflammation

To understand the progression of BBB disruption, we examined BBB permeability at various time points around when BBB disruption is observed following peripheral inflammation. We observed a slight increase in BBB permeability starting 3 hours after the final LPS injection, with evident BBB disruption observed at 6 hours post-injection. The BBB damage persisted for approximately 24 hours (Fig. 4 a, b).

Furthermore, we observed IL-1β cleavage in the brain lysates beginning at 3 hours following repeated LPS stimulation (Fig. 5 a, b). Similarly, IL-1β and IL-6 brain protein levels started to elevate from 3 hours after the LPS challenge (Fig. 5 c, d).

In contrast, myeloid cell infiltrations into the brain began at 5 hours post-LPS stimulation, with more robust infiltration occurring at 6 hours post-injection (Fig. 6 a, b). Consistent with our previous findings, we confirmed that the majority of these infiltrated cells were neutrophils (Fig 6 c). Collectively, these findings suggest that peripheral inflammation first triggers brain inflammation, followed by BBB disruption and immune cell infiltration.

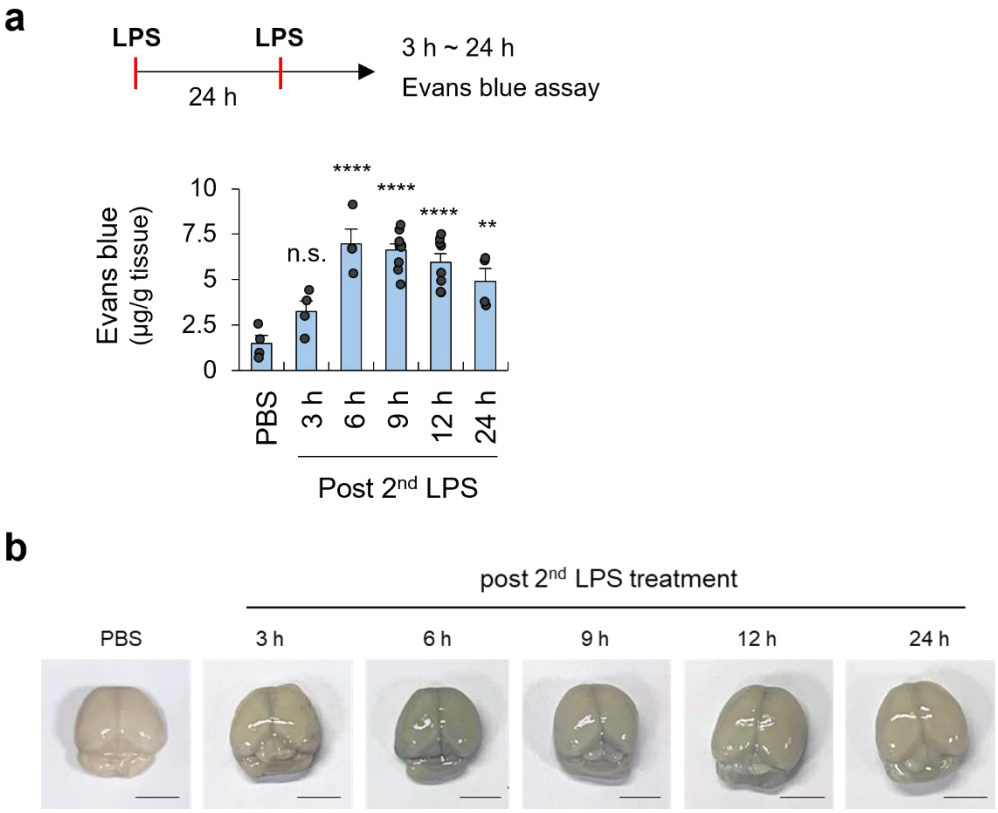

Fig 4. Peripheral inflammation-induced BBB disruption persists for up to 24 hours. (a) Schematic of experimental design to assess the duration of BBB disruption following LPS-induced brain inflammation in WT mice. Mice administered two intraperitoneal injections of LPS (0.8 mg/kg) in a 24 h interval. Evans blue dye was administered intravenously 1 h prior to sacrifice, and brain tissues were obtaianed at selected time points of 3, 6, 9, 12, and 24 hours after the final LPS injection. Quantification of Evans blue deposition per gram of brain tissue is shown. (n = 4 (PBS), 4 (3 h), 4 (6 h), 9 (9 h), 8 (12 h), 4 (24 h)). (b) Representative brain images from the Evans blue assay corresponding to (a). All animals were perfused to eliminate contamination of intravascular Evans blue dye. Scale bars = 0.5 cm. Differences among groups were performed through one-way ANOVA, subsequently analyzed using Dunnett's post hoc analysis, asterisk used to denote statistically significant differences. Results are shown as means ± SEM (a). $^{**}P < 0.01$, $^{****}P < 0.0001$, n.s. not significant.

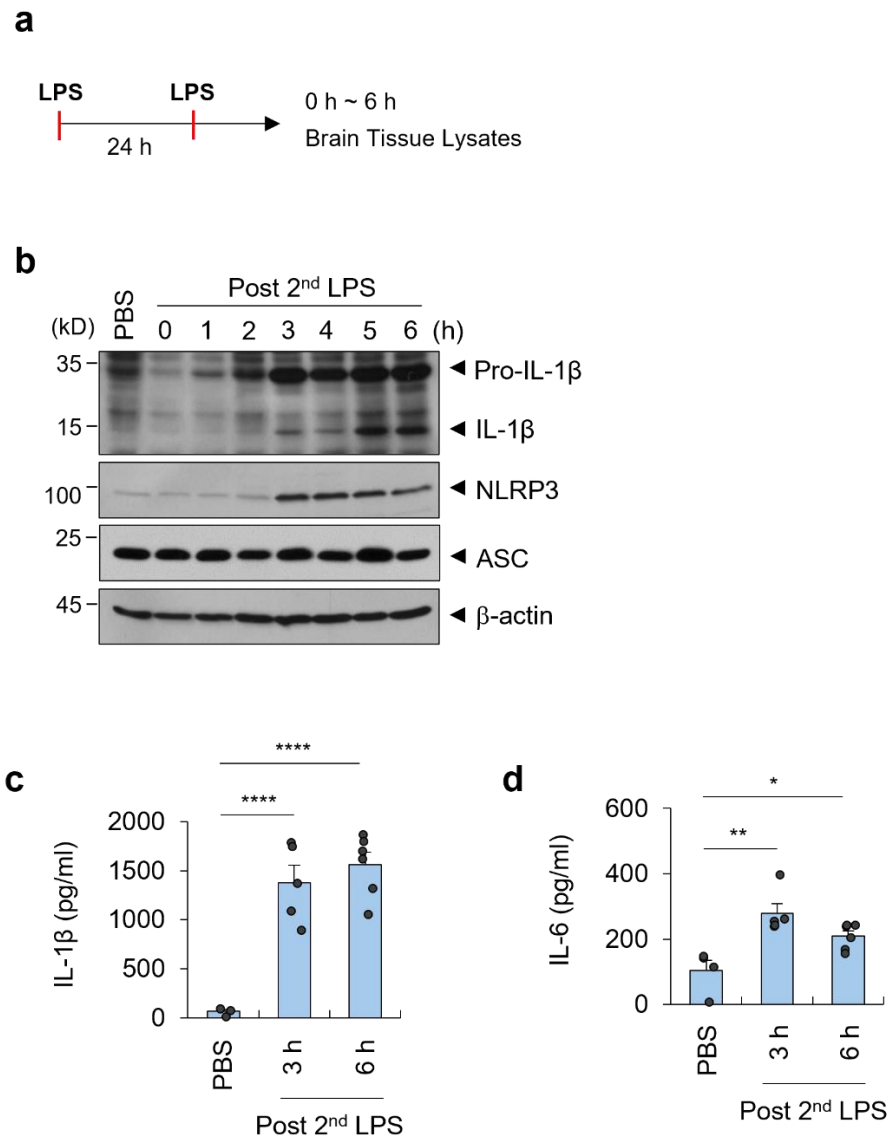

Fig 5. Brain inflammation precedes BBB disruption in response to peripheral inflammation. (a) Schematic of the experimental design to assess the temporal progression of brain inflammation following peripheral LPS administration. WT mice administered two intraperitoneal injections of LPS (0.8 mg/kg) in a 24 h interval. Brain tissues were harvested at multiple time points (0-6 h) upon the final LPS challenge. (b) Representative Immunoblot depicting the levels of pro-IL-1β, mature

IL-1β, NLRP3, and β-actin in lysates obtained from mouse brain treated as described in (a). (c, d) Quantitative measurement of IL-1β (c) and IL-6 (d) protein concentrations in brain lysates from mice injected with PBS or LPS, collected at 3 or 6 hours after the final injection measured by ELISA. (n = 4 (PBS), 5 (LPS 3 h), 6 (LPS 6 h)). Differences among groups were performed through one-way ANOVA, subsequently analyzed using Dunnett's post hoc analysis, asterisk used to denote statistically significant differences. Results are shown as means ± SEM (c, d). *$P < 0.05$, **$P < 0.01$, ****$P < 0.0001$, n.s. not significant.

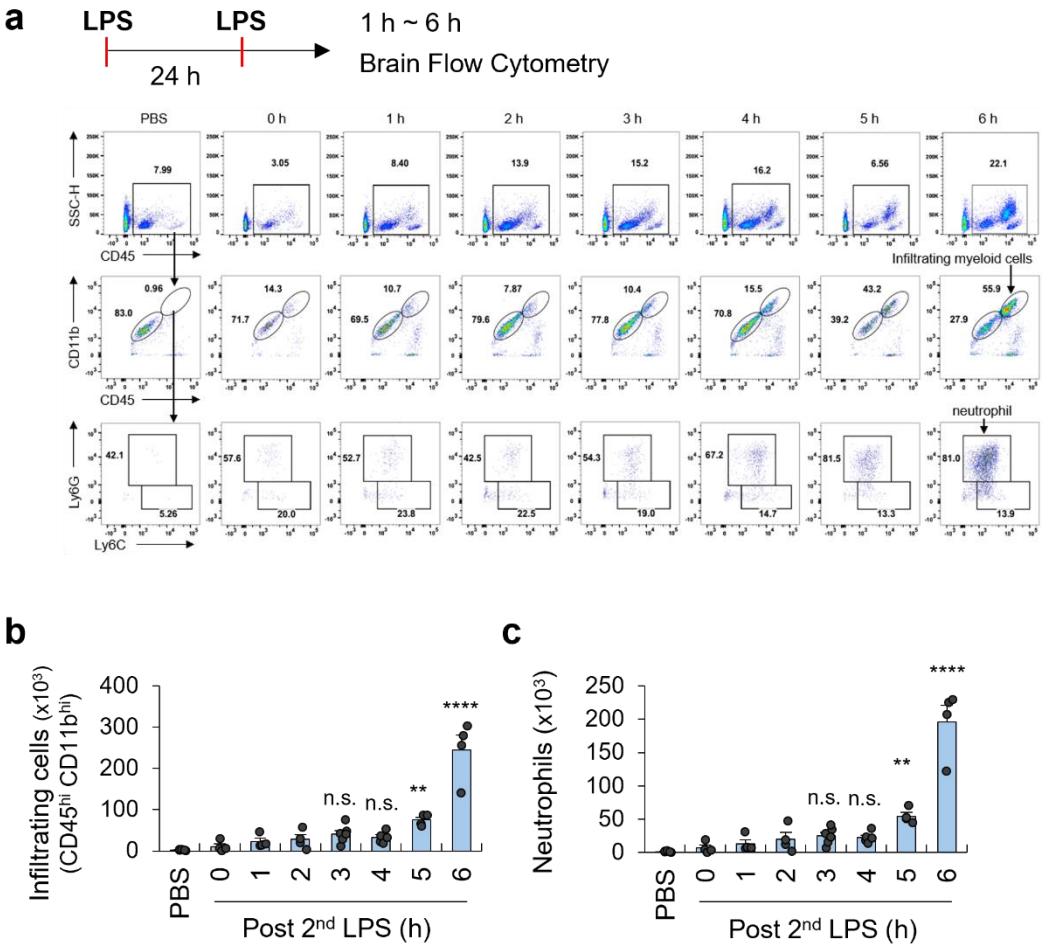

Fig 6. Immune cell infiltration following repeated LPS injection begins at 5 hours post injection. (a) Schematic of the experimental design to assess the temporal progression of brain immune cell infiltrations following peripheral LPS administration. WT mice administered two intraperitoneal injections of LPS (0.8 mg/kg) in a 24 h interval. Fresh brain tissues were collected for flow cytometry analyses at different time intervals (0-6 h). (b) Representative gating strategy illustrating the identification of total immune cells ($CD45^{+}$), microglia ($CD45^{int}$, $CD11b^{int}$), infiltrating myeloid populations ($CD45^{hi}$, $CD11b^{hi}$), neutrophils ($CD45^{hi}$, $CD11b^{hi}$, $Ly6C^{int}$, $Ly6G^{+}$), and monocytes ($CD45^{hi}$, $CD11b^{hi}$, $Ly6C^{+}$, $Ly6G^{-}$) in the brains of WT mice at different time intervals (0-6 hours post injection) is shown. (b, c) Quantitative measurement of infiltrating cells (b) and

neutrophils (c) in the brains of WT mice following LPS injections at different time points as described in (a). (b, c, n = 5 (PBS), 6 (3 h), 5 (4 h), 4 (all other group)). Differences among groups were performed through one-way ANOVA, subsequently analyzed using Dunnett's post hoc analysis, asterisk used to denote statistically significant differences. Results are shown as means ± SEM (b, c). $^{**}P < 0.01$, $^{****}P < 0.0001$, n.s. not significant.

3.3. The neutrophil-derived matrix metalloproteinases promote BBB disruption

Having identified neutrophils as the predominant infiltrating cells in the brain upon repeated LPS stimulation, we next determined their involvement in BBB disruption. Significant upregulation in mRNA levels of *Cxcl1*, *Cxcl2*, and *Cxcl3* chemokines in the brain were observed as early as 3 hours after the second LPS injection, indicating that the chemokine production occurs simultaneously with the onset of brain inflammation before the BBB disruption (Fig. 7 a-d).

To further investigate the direct roles of recruited neutrophils in influencing BBB integrity, we pretreated mice with CXCR2 antagonists or anti-Ly6G neutralizing antibodies before the LPS injection. As a result, both anti-Ly6G antibodies and CXCR2 antagonist treatment significantly attenuated BBB disruption following peripheral inflammation (Fig. 8 a, b). Next, we used *Ccr2*$^{-/-}$ mouse to investigate the potential role of recruited monocytes in driving BBB disruption. However, BBB integrity was unaffected in *Ccr2*$^{-/-}$ mice compared to the WT mice following peripheral inflammation (Fig. 8 c). Together, this data suggests that neutrophils, rather than monocytes, play indispensable roles in driving BBB disruption.

As it is previously reported that the matrix metalloproteinases (MMPs) can promote BBB disruption by directly degrading tight junction molecules or extracellular matrix (ECM) components[68,69], we observed the expression levels of *mmp8* and *mmp9* in brain tissue upon LPS stimulation (Fig. 9 a). Both *mmp8* and *mmp9* were significantly upregulated in the brain following LPS injection starting at 6 hours after the last LPS injection, and, consistently, MMP9 protein levels were significantly increased at the same time point (Fig. 9 b-d).

Additionally, the pretreatment of pan-MMP inhibitor, Ilomastat, before the second LPS injection significantly alleviated the BBB disruption as determined in Evans blue and NaF assay (Fig 10 a-c). Collectively, these findings demonstrate that neutrophil-derived MMPs are key molecules that promote BBB disruption.

These findings suggest that BBB disruption is not a direct consequence of inflammasome activation, but rather a result of a multistep process wherein microglial NLRP3 activation triggers the production of CXCL-related chemokines, which subsequently promote neutrophil recruitment and the adhesion to brain vasculature. Neutrophil-derived factors and upregulated extracellular matrix-modifying enzymes may contribute to the ultimate structural compromise of the BBB.

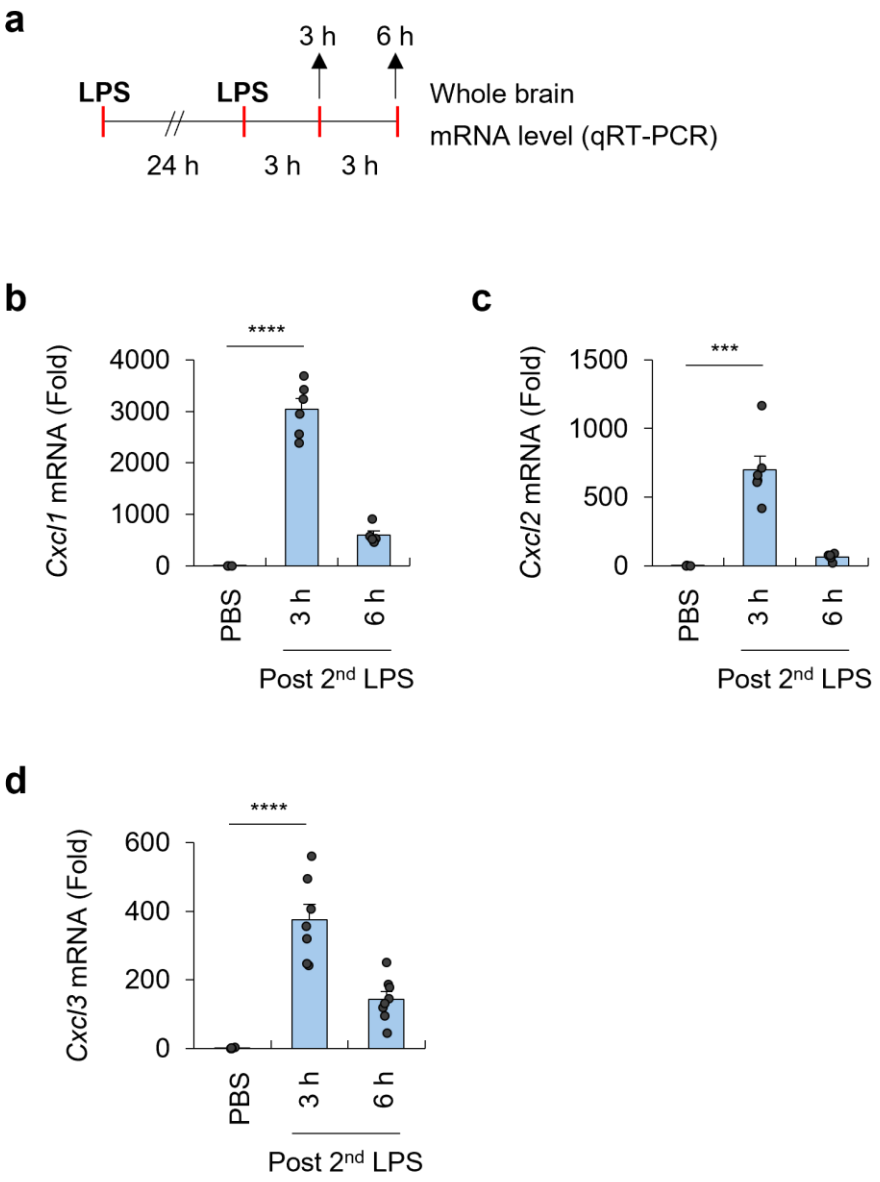

Fig 7. Peripheral inflammation triggers chemokine expressions in the brain at earlier time point. (a) Schematic of the experimental design to assess the comparative mRNA levels of chemokine expressions in the brain following peripheral LPS administration. WT mice administered two intraperitoneal injections of LPS (0.8 mg/kg) in a 24 h interval. Brain tissues were isolated at 3

h and 6 h after the final LPS challenge. (b, c, d) Measurement of transcript abundance of *Cxcl1* (b), *Cxcl2* (c), and *Cxcl3* (d) mRNA expression in the brain following repeated LPS injections (3 or 6 hours post last LPS injection) by quantitative RT-PCR. *Rn18s* was used as a control gene. (b, c, n = 3 (PBS), 6 (3 h), 5 (6 h); d, n = 5 (PBS), 7 (3 h), 8 (6 h)). Differences among groups were performed through one-way ANOVA, subsequently analyzed using Dunnett's post hoc analysis, asterisk used to denote statistically significant differences. Results are shown as means ± SEM (b, c, d). ***P < 0.001, ****P < 0.0001, n.s. not significant.

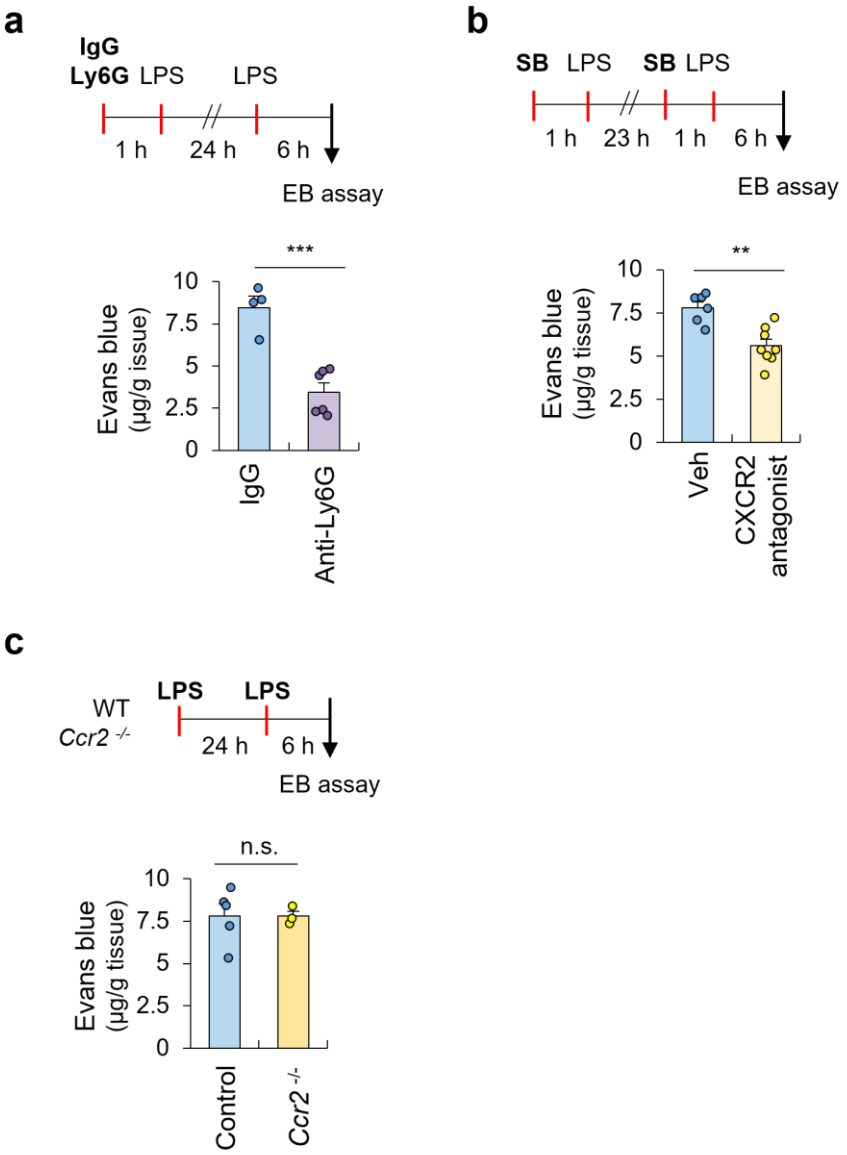

Fig 8. Neutrophil recruitment is critical in peripheral inflammation-driven BBB disruption. (a) Schematic of the experimental design of neutrophil depletion and LPS injections is shown. WT mice were pre-administered with intraperitoneal injections of anti-Ly6G antibody (50 mg/kg) or control IgG 1 h before the LPS injection. After 6 hours of two intraperitoneal injections of LPS (0.8

mg/kg; 24 h interval), brain tissues were collected for Evans blue assay. Evans blue dye was administered intravenously 1 h before tissue collection. Quantification of Evans blue deposition per gram of brain tissues pretreated with IgG or anti-Ly6G antibodies following repeated LPS injections is shown. (n = 4 (IgG), 6 (anti-Ly6G)). (b) Schematic of the experimental design of CXCR2 antagonist (SB225002; SB) administration and LPS injection is shown. WT mice were pre-administered with intraperitoneal injections of SB (2 mg/kg) or vehicle (Veh) before each LPS injection, and brain tissues were harvested for Evans blue assay. Quantification of Evans blue deposition per gram of brain tissues of Veh or SB-pretreated mice following repeated LPS injections is shown. (n= 6 (Veh), 8 (SB)). (c) Schematic of the experimental design of LPS injection in WT and *Ccr2*$^{-/-}$ mice is shown. WT and *Ccr2*$^{-/-}$ mice administered two intraperitoneal injections of LPS (0.8 mg/kg) in a 24 h-interval, and brain tissues were collected for Evans blue assay at 6 h post final LPS injection. Measurement of Evans blue leakage in brain tissues of WT and *Ccr2*$^{-/-}$ mice following repeated LPS injection is shown (n= 5 (WT), 3 (CCR2$^{-/-}$)). Differences among groups were performed through a two-tailed t-test assuming unequal group pairing, asterisk used to denote statistically significant differences. Results are shown as means ± SEM (a, b, c). $^{**}P < 0.01$. $^{***}P < 0.001$, n.s. not significant.

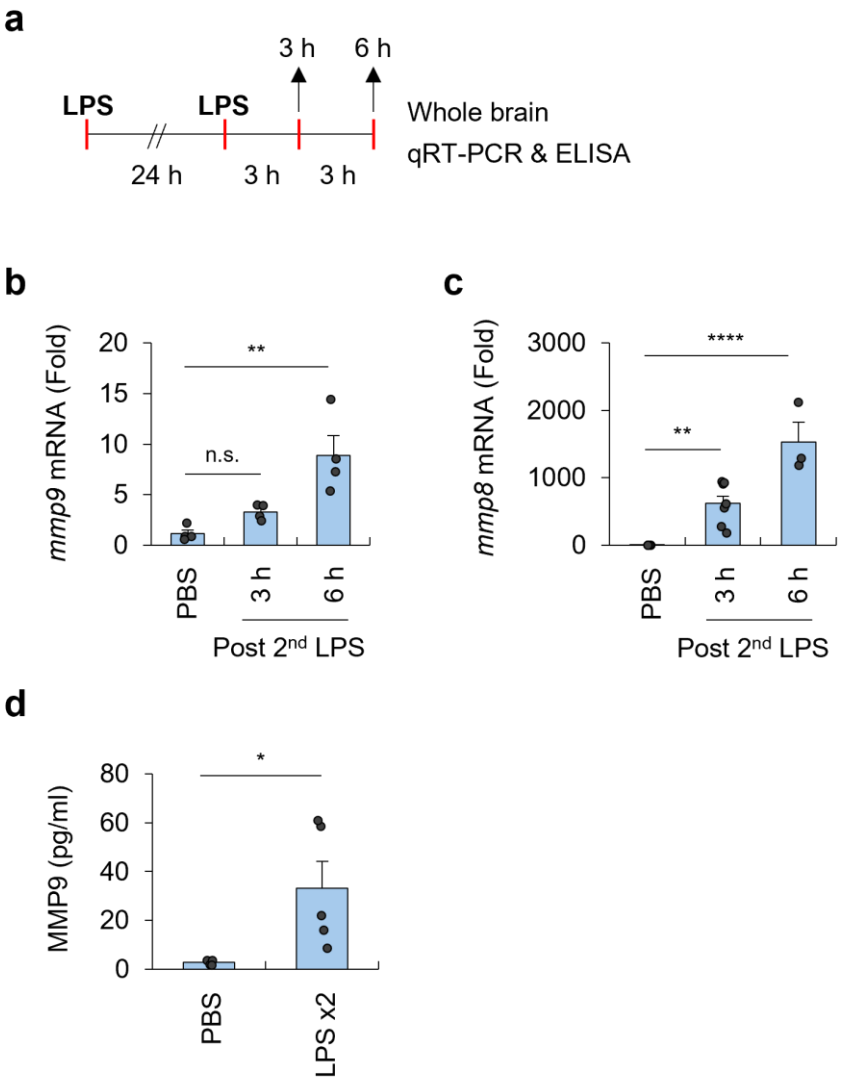

Fig 9. Peripheral inflammation triggers matrix metalloproteinases expressions in the brain followed by BBB disruption. (a) Schematic of the experimental design to assess the MMP levels in the brain following peripheral LPS administration. WT mice administered two intraperitoneal injections of LPS (0.8 mg/kg) in a 24 h interval. Brain tissues were harvested at 3 h and 6 h after the final LPS administration. (b, c) Quantitative measurement of comparative *Mmp9* (b) and *Mmp8* (c) mRNA levels in the brain following repeated LPS injections in WT mice using qRT-PCR (3 or 6

hours post last LPS injection). (d) Quantification of MMP9 protein levels in the brain lysates 6 hours following repeated LPS injection in WT mice using ELISA. (b, n = 4 (PBS), 4 (3 h), 4 (6 h); c, n = 5 (PBS), 8 (3 h), 3 (6 h); d, n = 5). Differences among groups were performed through one-way ANOVA, subsequently analyzed using Dunnett's post hoc analysis or a two-tailed t-test assuming unequal group pairing, asterisk used to denote statistically significant differences. Results are shown as means ± SEM (b, c, d). *$P < 0.05$, **$P < 0.01$, ****$P < 0.0001$, n.s. not significant.

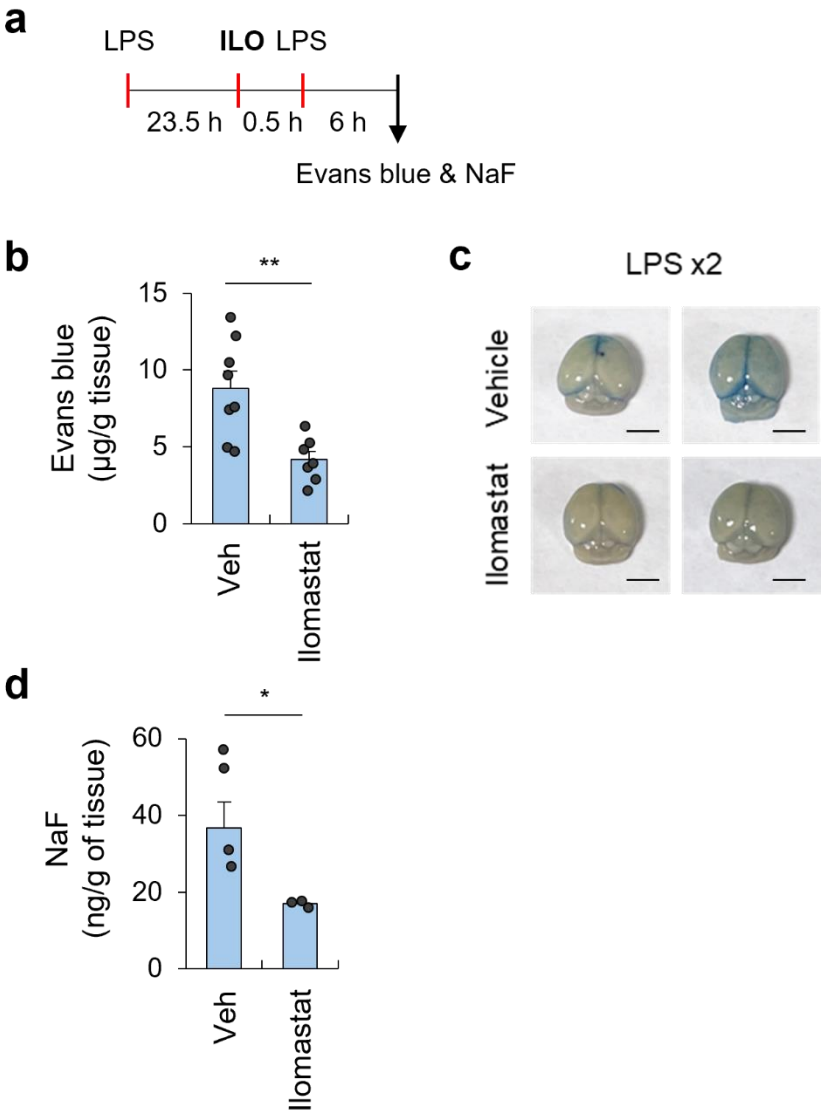

Fig 10. Matrix metalloproteinases inhibition alleviates peripheral inflammation-induced BBB disruption. (a) Schematic of the experimental design to assess the administration of pan-MMP inhibitor (Ilomastat) and LPS injections is shown. Ilomastat is intraperitoneally injected 30 min prior to the second LPS (0.8 mg/kg) injection, and tissues were harvested at 6 h after the final LPS administration. (b) Quantification of Evans blue deposition per gram of brain tissue in WT mice pre-

treated with Ilomastat following repeated LPS injections is shown. (n = 8 (Veh), 7 (Ilomastat)). (c) Representative brain images from the Evans blue assay corresponding to (b). Scale bars = 0.5 cm. (n = 8 (Veh), 7 (Ilomastat)). (d) Quantification of NaF leakage per gram of brain tissue in WT mice pre-treated with Ilomastat following repeated LPS injections. Evans blue or NaF were intravenously injected 1 h before sacrifice, and all animals were perfused to eliminate the contamination of intravascular Evans blue dye or NaF. (n = 4 (Veh), 3 (Ilomastat)). Differences among groups were performed through a two-tailed t-test assuming unequal group pairing, asterisk used to denote statistically significant differences. Results are shown as means ± SEM (a, b, c). *P < 0.05, **P < 0.01, n.s. not significant.

3.4. BBB disruption upon peripheral inflammation occurs in an NLRP3-dependent manner

To elucidate the molecular mechanism underlying BBB impairment induced by peripheral inflammation, we performed single-cell RNA sequencing on mouse brain tissue (Fig. 11 a). We identified 16 clusters in mouse brain as determined in the Uniform Manifold Approximation and Projection (UMAP) (Fig. 11 b). Remarkably, brain-resident microglia, infiltrating neutrophils, and monocyte-derived macrophages (Mo-Mac) within the brain showed increased levels of inflammasome components (Fig. 11 c, d).

Given that repeated LPS stimulation might activate NLRP3 inflammasome in the mouse brain, we analyzed BBB permeability, brain inflammation, immune cell infiltration, and glial cell activation in *Nlrp3*$^{-/-}$ mice. As a result, repeated LPS administration resulted in significantly reduced Evans blue and NaF leakage into the brain in *Nlrp3*$^{-/-}$ mice (Fig. 12 a-d). It is previously demonstrated that cytokine treatment, such as TNFα, IL-1β, or IL-6 can promote loss in tight junction molecules or cellular damages *in vitro*[48,70]. Therefore, we next evaluated whether peripheral cytokine productions in the plasma serve as contributing factors to the peripheral inflammation-induced BBB disruption. We administered the cytokine cocktail (IL-1β, IL-6, and TNFα) intravenously in WT and *Nlrp3*$^{-/-}$ mice to mimic the peripheral cytokine productions instead of LPS administration. As a result, we observed a dramatic increase in BBB permeability following cytokine injections; however, this effect is abolished in *Nlrp3*$^{-/-}$ mice. This suggests that NLRP3 inflammasome activation, rather than systemic cytokine production alone, plays a more direct and critical role in triggering BBB disruption.

Also, repeated LPS injections induced IL-1β maturation in the brain in an NLRP3-dependent mechanism (Fig. 13 a, b). To confirm the involvement of NLRP3 inflammasome in BBB permeability induced by peripheral inflammation, we utilized a caspase-1 activatable fluorescent probe[65]. Caspase-1 activation was observed in peripheral tissues, including the lung and spleen, following a single LPS injection. In contrast, activation of caspase-1 in the brain occurred only after two repeated LPS injections, but not after a single LPS injection (Fig 13 e, f). Collectively, we observed NLRP3 inflammasome activation in the brain upon peripheral inflammation-induced BBB disruption. Furthermore, in response to LPS exposure, *Nlrp3*$^{-/-}$ mice exhibited diminished

brain pro-inflammatory cytokines levels compared to WT mice following peripheral LPS challenge (Fig. 13 c, d).

Consistently, *Nlrp3* deficiency markedly attenuated the increase of brain-infiltrating myeloid populations induced by peripheral LPS administration (Fig. 14 a-f). Importantly, the infiltration of neutrophils, which were determined to promote BBB disruption by MMP productions, was significantly reduced in *Nlrp3*$^{-/-}$ mice following repeated LPS injections (Fig. 14 e).

To further investigate changes in the reactivity of brain resident glial cells, we performed immunohistochemistry (IHC)-based image analyses on astrocytes and microglia of hippocampal regions from WT and *Nlrp3*$^{-/-}$ mice following repeated LPS injections (Fig. 15 a). We observed an increase in GFAP and Iba1 fluorescence intensity in WT mice upon peripheral inflammation, each indicating profound gliosis in astrocytes and microglia, respectively; however, the glial cell reactivity was markedly alleviated in *Nlrp3*$^{-/-}$ mice (Fig. 15 b, c, e). In WT mice, the number in astrocytes was elevated in response to LPS injections, which was abrogated in *Nlrp3*$^{-/-}$ mice (Fig. 15 d). The cell number of microglia was not affected by LPS injections in both WT and *Nlrp3*$^{-/-}$ mice in consistent with the flow cytometry analysis (Fig. 15 f). Therefore, we concluded that NLRP3 inflammasome activation plays a crucial role in driving the peripheral inflammation-induced BBB impairment.

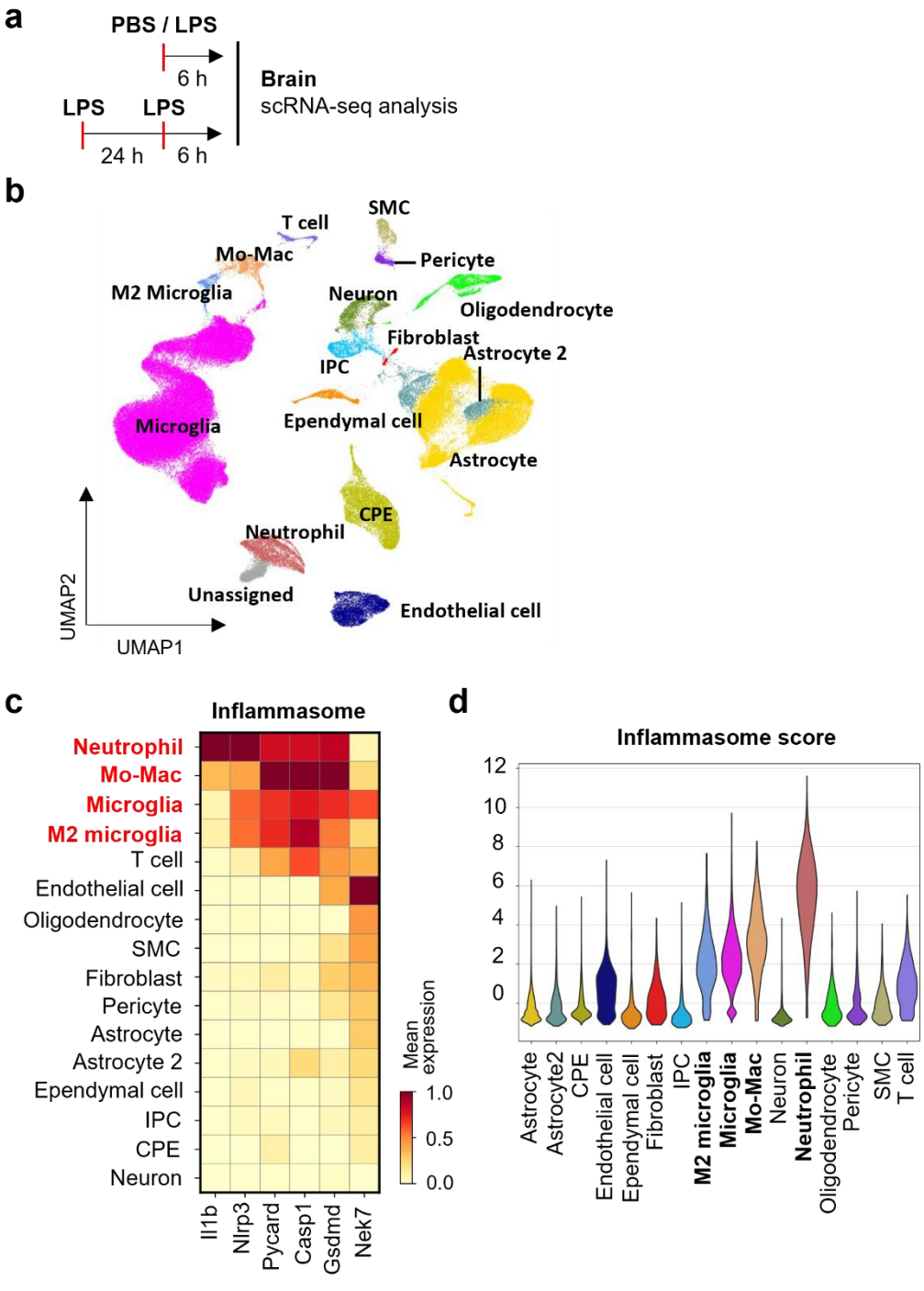

Fig 11. Single-cell transcriptomic analysis reveals upregulation of inflammasome-associated gene expressions in mouse brain following LPS stimulation. (a) Experimental design schematic procedure for single-cell RNA sequencing (scRNA-seq). WT mice were administered PBS or LPS intraperitoneally at 0.8 mg/kg, one or two times with a 24 h interval. Brain tissues were isolated 6 h post-final challenge and processed for scRNA-seq analysis. (b) UMAP plots showing distinct clusters in the mouse brain based on scRNA-seq data, encompassing 105,838 gene expression profiles. (c) Heatmap displaying the inflammasome-associated gene expression profiles across individual cell cluster with color intensity reflecting the scaled average expression. (d) VISION-based scoring of inflammasome genes set across all cell clusters, represented by a violin plot showing the distribution of inflammasome score.

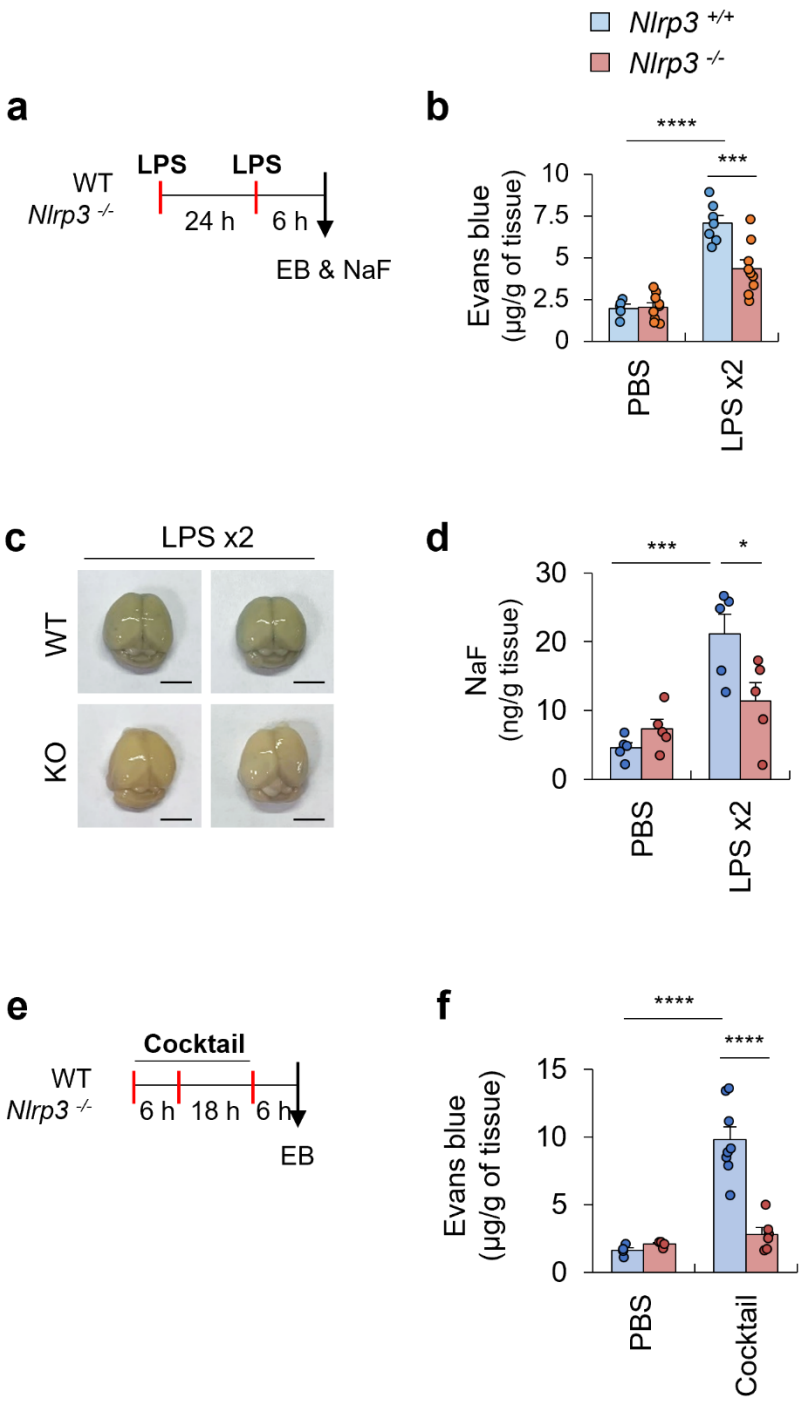

Fig 12. BBB disruption following repeated LPS injection is NLRP3-dependent. (a) Schematic of the experimental design for BBB permeability assay in WT and *Nlrp3*$^{-/-}$ mice following repeated LPS injection. WT and *Nlrp3*$^{-/-}$ mice were intraperitoneally injected with LPS twice in a 24 h interval, and Evans blue or NaF assay were performed at 6 h post LPS injections. (b) Quantitative measurement of Evans blue deposition per gram of brain tissue from WT and *Nlrp3*$^{-/-}$ mice following repeated LPS injection. (n = 5 (WT PBS), 7 (WT LPS x2), 9 (*Nlrp3* KO)). (c) Representative brain image of Evans blue assay done in (b). Scale bars = 0.5 cm. (d) Quantification of NaF leakage per gram of brain tissues from WT and *Nlrp3*$^{-/-}$ mice following repeated LPS injection. (n = 5 per group). (e) Schematic of the experimental design for BBB permeability assay in WT and *Nlrp3*$^{-/-}$ mice following cytokine injection. f) Quantification of Evans blue deposition per gram of brain tissues from WT and *Nlrp3*$^{-/-}$ mice following intravenous injection of cytokine cocktail containing IL-1β at 10 μg/kg, TNF-α at 35 μg/kg, and IL-6 at 35 μg/kg. (n = 4 per group). Differences among groups were performed through two-way ANOVA, subsequently analyzed using Bonferroni multiple comparisons test, asterisk used to denote statistically significant differences. Results are shown as means ± SEM (b, d, e). *$P < 0.05$, ***$P < 0.001$, ****$P < 0.0001$.

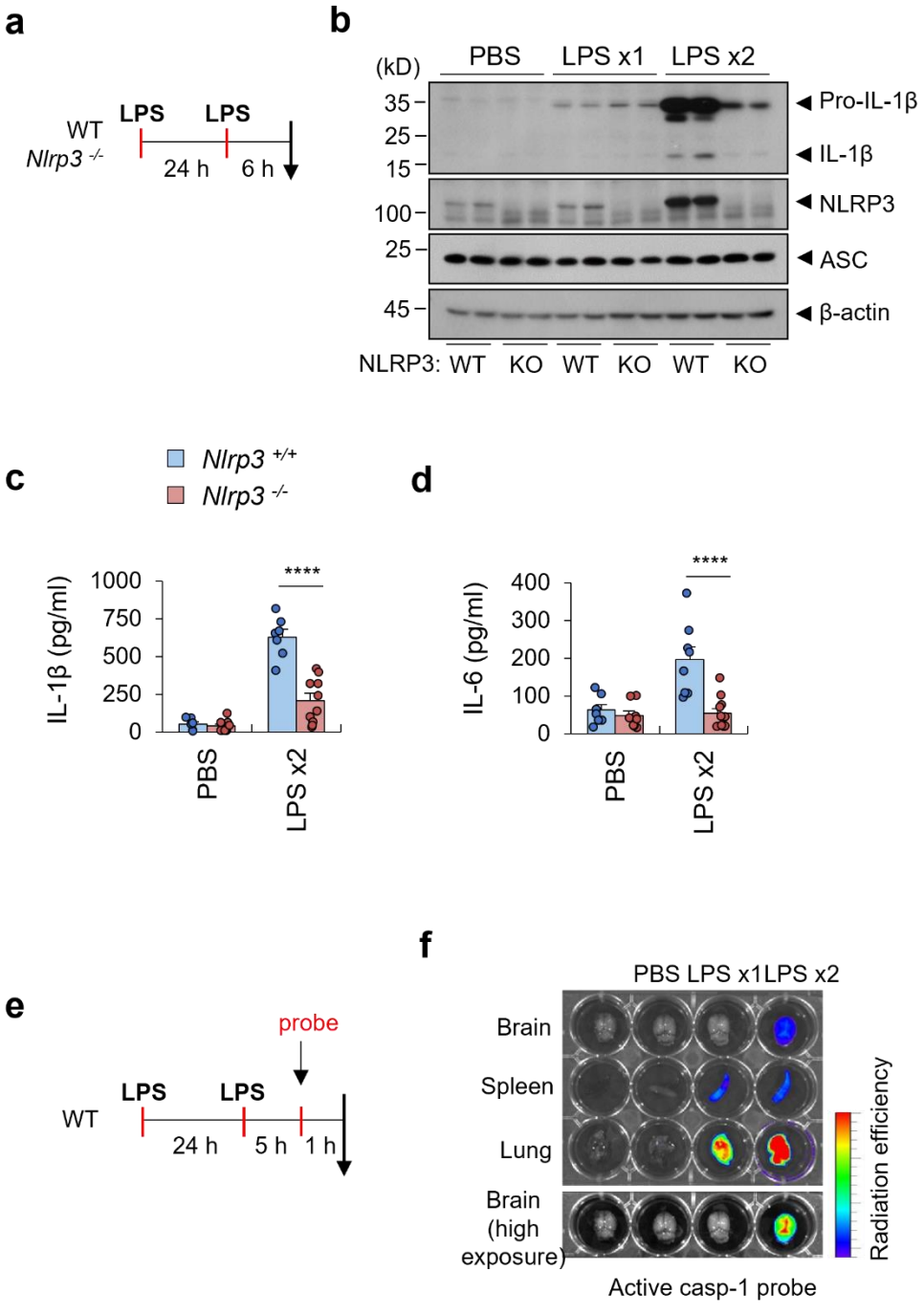

Fig 13. NLRP3 inflammasome is activated in the brain following repeated LPS injection. (a) Schematic of experimental design for LPS-induced brain inflammation in WT and *Nlrp3*$^{-/-}$ mice. Mice administered two intraperitoneal injections of LPS (0.8 mg/kg; 24 h interval). Brain tissues were isolated 6 h after the final LPS treatment for ELISA and Immunoblot analysis to assess NLRP3 inflammasome activity. (b) Representative immunoblots of brain lysates detecting pro-IL-1β, mature IL-1β, NLRP3, ASC, and β-actin from WT and *Nlrp3*$^{-/-}$ mice following PBS or LPS injection (6 h post last injection). (c, d) Quantitative measurement of IL-1β (c) and IL-6 (d) protein expressions in brain lysates from WT and *Nlrp3*$^{-/-}$ mice following PBS or LPS injection (6 h post last injection) using ELISA. (c, n = 6 (WT PBS), 7 (WT LPS x2), 9 (KO, PBS), 10 (KO, LPS x2); d, n = 7 (WT PBS), 8 (WT LPS x2), 8 (KO, PBS), 11 (KO, LPS x2)). (e) Schematic of experimental design for in vivo detection of active caspase-1 in WT mice in response to peripheral inflammation. Mice administered two intraperitoneal injections of LPS (0.8 mg/kg; 24 h interval), followed by intravenous administration of a fluorescence-conjugated active caspase-1 probe 1 h before tissue collection. Brain, spleen, and lung tissues were harvested for ex vivo imaging. (f) *Ex vivo* images showing active caspase-1 detection in the brain (low and high exposure), spleen, and lung tissues as described in (e). Differences among groups were performed through two-way ANOVA, subsequently analyzed using Bonferroni multiple comparisons test, asterisk used to denote statistically significant differences. Results are shown as means ± SEM (c, d). ****$P < 0.0001$.

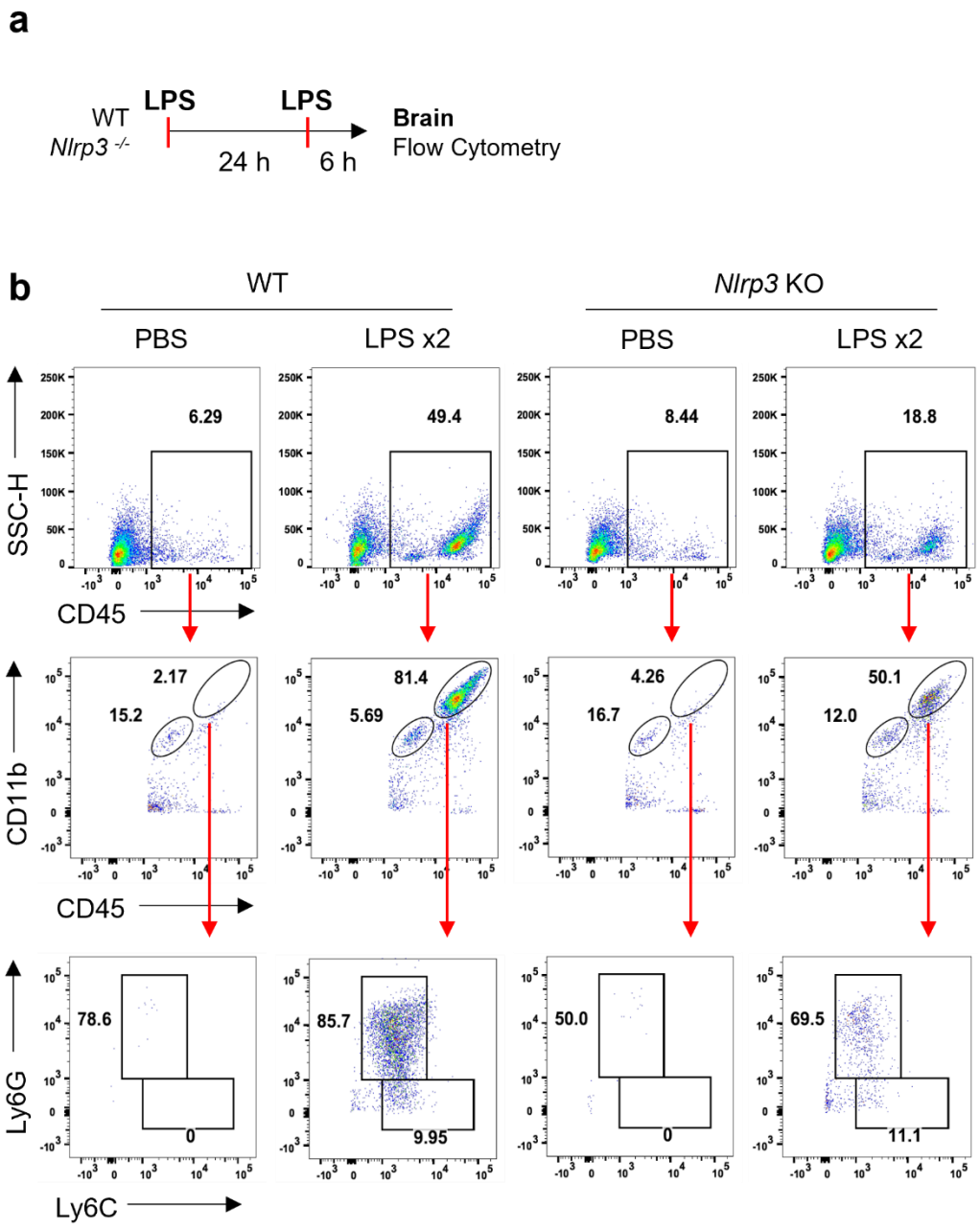

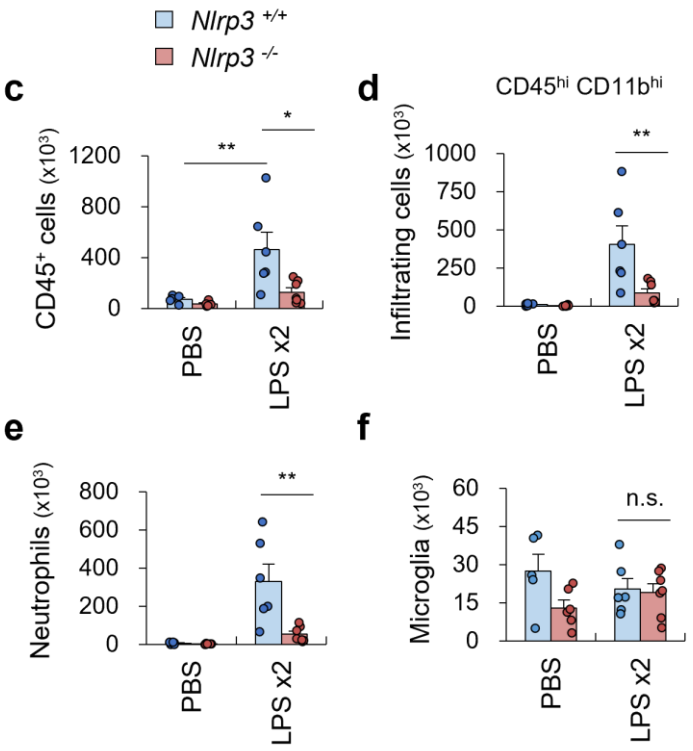

Fig 14. Immune cell infiltrations in the brain following repeated LPS injection is highly NLRP3-dependent. (a) Schematic of the experimental design for LPS-induced brain inflammation in WT and *Nlrp3*$^{-/-}$ mice. Mice administered two intraperitoneal injections of LPS (0.8 mg/kg; 24 h interval). Fresh brain tissues were harvested 6 h post the final LPS injection for flow cytometry analysis. (b) Representative gating strategy illustrating the identification of immune cells (CD45^{+}), microglia (CD45^{int}, CD11b^{int}), infiltrating myeloid cells (CD45^{hi}, CD11b^{hi}), neutrophils (CD45^{hi}, CD11b^{hi}, Ly6C^{int}, Ly6G^{+}), and monocytes (CD45^{hi}, CD11b^{hi}, Ly6C^{+}, Ly6G^{-}) in WT or *Nlrp3*$^{-/-}$ mouse brains after PBS or LPS injections. (c, d, e, f) Quantification by flow cytometry of immune populations (c), infiltrating populations (d), neutrophils (e), and microglia (f) in WT and *Nlrp3*$^{-/-}$ mouse brain as described in (a). (n = 5 (WT PBS), 6 (WT LPS x2), 6 (KO PBS), 7 (KO LPS x2)). Differences among groups were performed through two-way ANOVA, subsequently analyzed using Bonferroni multiple comparisons test, asterisk used to denote statistically significant differences. Results are shown as means ± SEM (c, d, e, f). *$P < 0.05$, **$P < 0.01$, n.s. not significant.

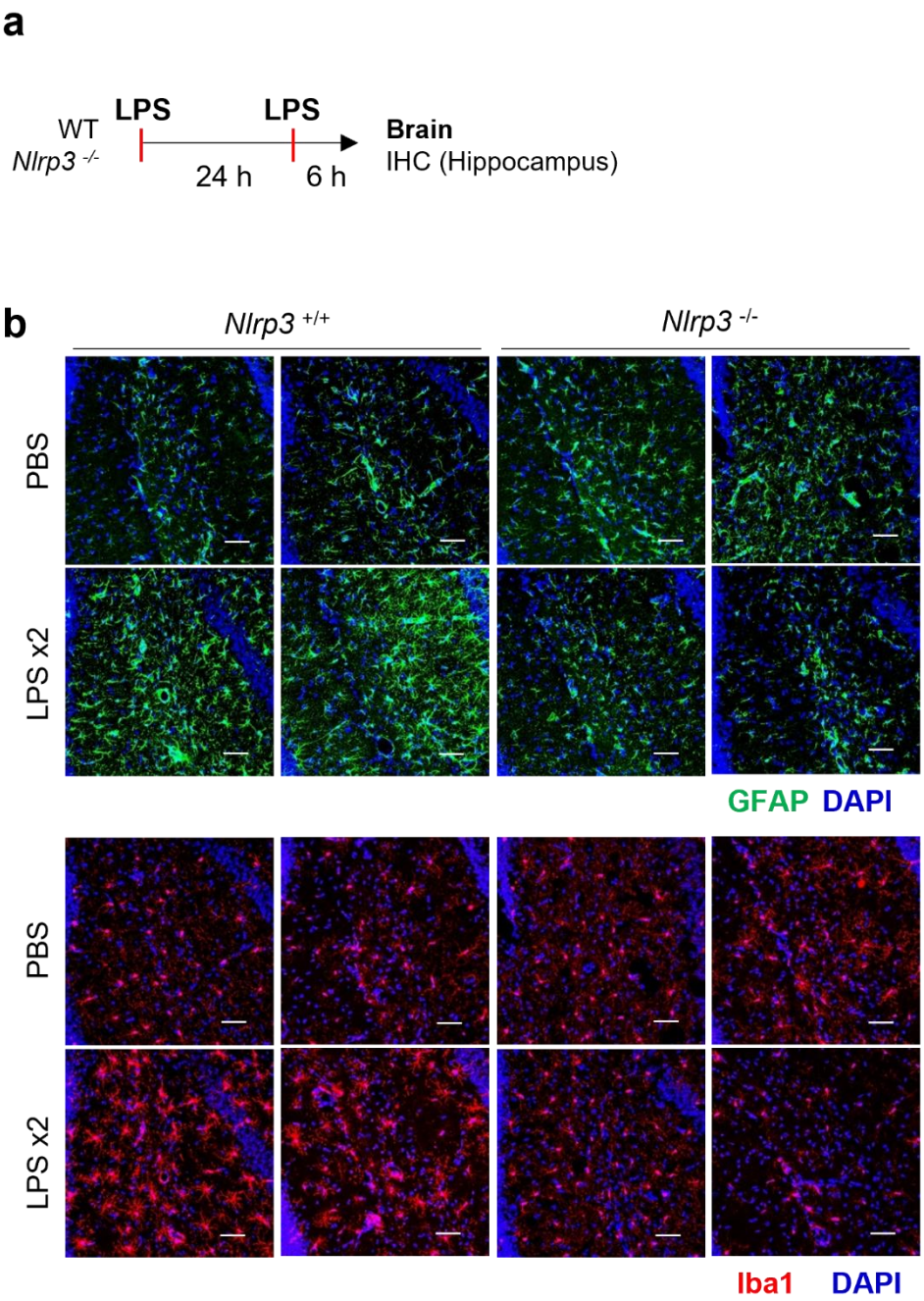

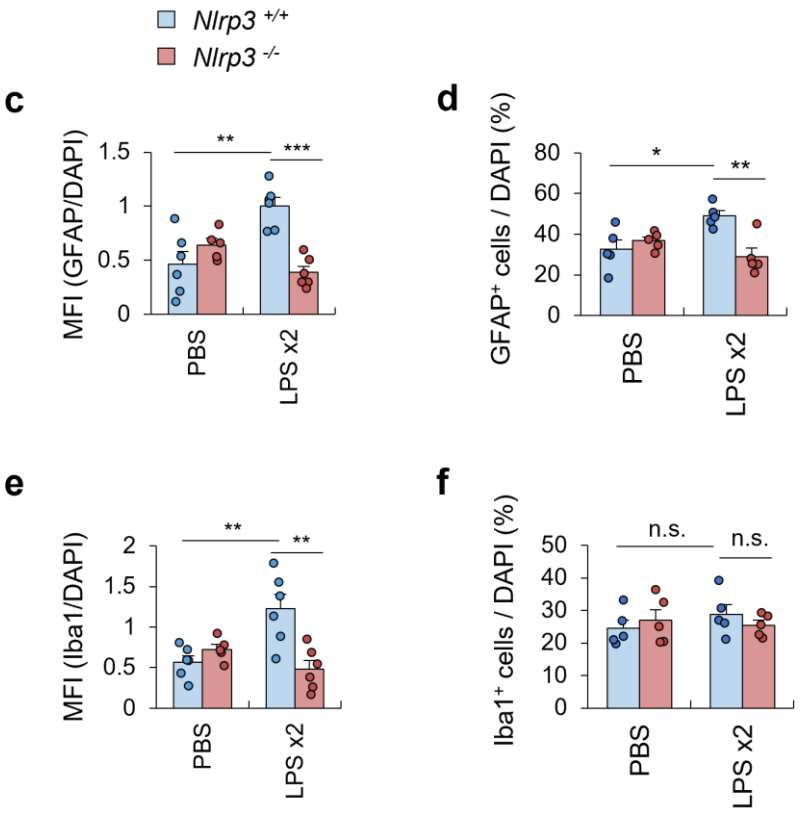

Fig 15. Gliosis in response to peripheral inflammation occurs in an NLRP3-dependent manner. (a) Schematic of the experimental design for LPS-induced brain inflammation in WT and *Nlrp3*$^{-/-}$ mice. Mice administered two intraperitoneal injections of LPS (0.8 mg/kg; 24 h interval). Brain tissues were harvested 6 h post the final LPS injection for confocal imaging. (b) Representative IHC images visualizing astrocytes (GFAP^{+}, green) and microglia (Iba1^{+}, red) from WT or *Nlrp3*$^{-/-}$ mice following PBS or LPS injections as described in (a). Images shown are the hippocampal regions of coronal brain sections. Scale bars= 50 μm. (c, d, e, f) MFI of GFAP (c) and Iba1 (e) and quantification of astrocytes (d) and microglia (f) cell counts normalized to DAPI as described in (a). (n = 6 (WT PBS), 6 (WT LPS x2), 5 (KO PBS), 6 (KO LPS x2)). Differences among groups were performed through two-way ANOVA, subsequently analyzed using Bonferroni multiple comparisons test, asterisk used to denote statistically significant differences. Results are shown as means ± SEM (c, d, e, f). *$P < 0.05$, **$P < 0.01$, ***P< 0.001, n.s. not significant.

3.5. NLRP3-gasdermin D axis drives peripheral inflammation-induced BBB disruption in an IL-1β -independent manner

Upon activation of the NLRP3 inflammasome, sensor molecules such as pyrin and NLRP3 assemble into the inflammasome complex[71]. This assembly activates caspase-1, subsequently promoting the gasdermin D (GSDMD) pore formation on the plasma membrane, facilitating the release of active IL-1β and IL-18 forms[67]. Therefore, we used *Gsdmd*$^{-/-}$ mice to investigate the role of GSDMD pore formation in peripheral LPS-induced BBB disruption (Fig. 16 a). Notably, *Gsdmd* deficiency significantly reduced the leakage of Evans blue and NaF into the brain following peripheral LPS injection (Fig. 16 b, c). This suggests that the GSDMD-mediated release of inflammatory mediators might trigger the peripheral inflammation-induced BBB disruption.

As shown in previous data, we found that repeated LPS injections induced NLRP3-dependent IL-1β cleavage in the brain, whereas IL-18 remained unaffected. To further examine the involvement of GSDMD-derived IL-1β in BBB disruption, we evaluated the BBB permeability and immune cell infiltrations in *Il1r1*$^{-/-}$ mice (Fig. 17 a). Surprisingly, peripheral LPS-induced Evans blue leakage in the brain occurred in an IL-1R signaling-independent manner (Fig. 17 b, c). Also, the myeloid cell infiltrations into the brain following peripheral inflammation were comparable between WT and *Il1r1*$^{-/-}$ mice (Fig. 17 d, e). Collectively, despite IL-1β being the key component released upon NLRP3 inflammasome activation, IL-1β is not essential in promoting BBB disruption induced by peripheral inflammation.

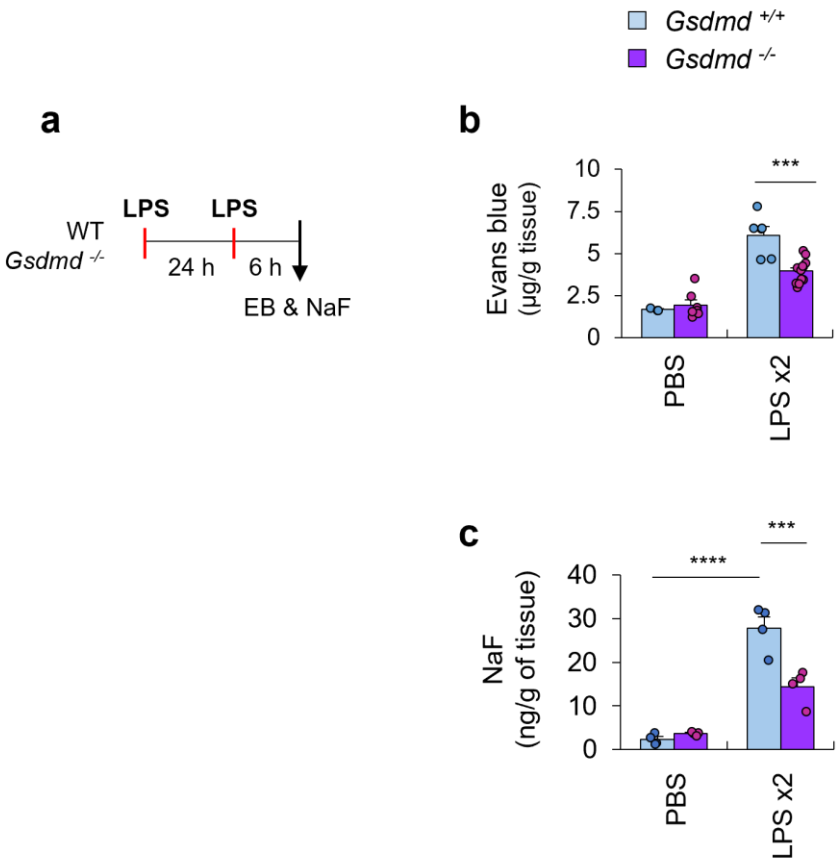

Fig 16. *Gsdmd*$^{-/-}$ abolishes peripheral inflammation-induced BBB disruption. (a) Experimental design schematic for BBB permeability assay in WT and *Gsdmd*$^{-/-}$ mice following repeated LPS injection. WT and *Gsdmd*$^{-/-}$ mice were intraperitoneally injected with LPS twice in a 24 h interval, and Evans blue or NaF assay were performed at 6 h post LPS injections. (b) Quantitative measurement of Evans blue deposition per gram of brain tissue from WT and *Gsdmd*$^{-/-}$ mice following repeated LPS injection as described in (a). (n = 3 (WT PBS), 6 (WT LPS x2), 7 (KO PBS), 12 (KO LPS x2)). (c) Quantification of NaF leakage per gram of brain tissues from WT and *Gsdmd*$^{-/-}$ mice following repeated LPS injection as described in (a). (n = 5 per group). Differences among groups were performed through two-way ANOVA, subsequently analyzed using Bonferroni multiple comparisons test, asterisk used to denote statistically significant differences. Results are shown as means ± SEM (b, c). ***P< 0.001, ****P< 0.0001, n.s. not significant.

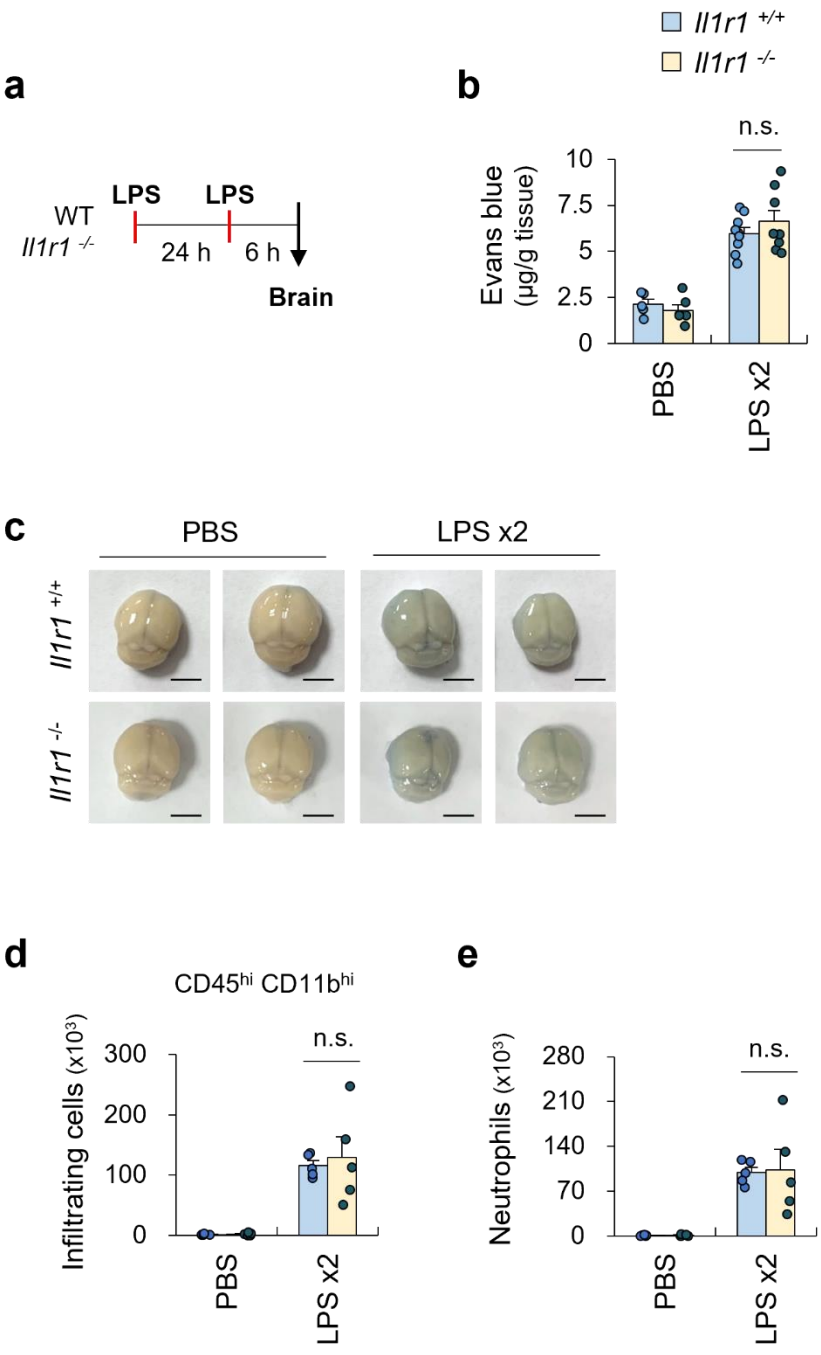

Fig 17. Peripheral inflammation-induced BBB disruption occurs in an IL-1R signaling-independent manner. (a) Schematic of the experimental design for peripheral inflammation-induced BBB disruption in WT and *Il1r1*$^{-/-}$ mice following repeated LPS injection. WT and *Il1r1*$^{-/-}$ mice were intraperitoneally injected with LPS twice in a 24 h interval. Fresh brain tissues were isolated 6 h after the final LPS administration, and Evans blue dye was administered through the tail vein 1 h prior to sacrifice. (b) Quantification of Evans blue deposition per gram of brain tissue from WT and *Il1r1*$^{-/-}$ mice following repeated LPS injection as described in (a). (n = 5 (WT PBS), 9 (WT LPS x2), 6 (KO PBS), 8 (KO LPS x2)). (c) Representative brain images of Evans blue assay performed in (b). (d, e) Flow cytometry-based quantification of infiltrating cells (CD45^{hi}, CD11b^{hi}) (d) and neutrophils (CD45^{hi}, CD11b^{hi}, Ly6C^{int}, Ly6G^{+}) (e) in WT and *Il1r1*$^{-/-}$ mouse brain as described in (a). (n = 5 per group). Differences among groups were performed through two-way ANOVA, subsequently analyzed using Bonferroni multiple comparisons test, asterisk used to denote statistically significant differences. Results are shown as means ± SEM (b, d, e). n.s. not significant.

3.6. Microglial NLRP3-gasdermin D axis is critical in triggering BBB disruption upon peripheral inflammation

To further understand the mechanism underlying NLRP3-GSDMD-mediated BBB disruption, we generated the transgenic mice expressing various cell type-specific hyperactive NLRP3 mutant-expressing (D301N) mice, in which the active form of NLRP3 is constitutively expressed[63]. We utilized the Cre-Lox system to generate mice expressing the hyperactive NLRP3 mutant specifically in CX3CR1-positive cells, including most myeloid cells and microglia, upon tamoxifen administration. Remarkably, these mice showed a notable increase in Evans blue leakage following peripheral LPS treatment, indicating that NLRP3 in microglia and other myeloid cells plays a key role in inducing BBB disruption (Fig. 18 a). However, when the hyperactive NLRP3 mutant was expressed specifically in astrocytes (Aldh1l1^{+} cells), no significant effect on peripheral LPS-induced BBB impairment was observed (Fig. 18 b). To investigate the contribution of microglial-specific NLRP3 activation to BBB disruption, we used Tmem119-speicific NLRP3 mutant expressing mice. Tamoxifen injection in these mice led to exclusive expression of the NLRP3 mutant in microglia, without affecting neutrophils or monocytes. Importantly, repeated LPS injections lead to markedly elevated Evans blue leakage in microglial NLRP3 mutant mice, underscoring the roles of microglial NLRP3 inflammasome in regulation of BBB integrity (Fig. 18 c). Moreover, to investigate the involvement of microglial GSDMD pore formation in BBB disruption, we established mice with microglial-specific deletion of *Gsdmd* (*Tmem119-CreER; Gsdmd fl/fl*). After tamoxifen administration, the absence of GSDMD in microglia significantly attenuated Evans blue extravasation following repeated LPS injection (Fig. 18 d). These findings indicate that NLRP3-GSDMD signaling within microglia is a major driver of mediating BBB compromise under conditions of repeated peripheral inflammation.

To evaluate the changes in *Cxcl* chemokine expression, we measured the gene expression of *Cxcl1* and *Cxcl2* in *Gsdmd*-, *Nlrp3*-, and *Il1r1*-deficient mice (Fig. 19 a). In line with the observed alterations in BBB integrity in each transgenic mice, upregulations of *Cxcl* chemokines were highly dependent on NLRP3-GSDMD axis but independent of IL-1R signaling (Fig. 19 b, c). To further confirm this, we also observed a marked decrease in the *Cxcl* chemokine mRNA levels

following repeated LPS injections in microglial-specific Gsdmd deficient mice, indicating the involvement of microglial NLRP3-GSDMD axis in inducing chemokine expressions in the brain following peripheral inflammation (Fig. 19 d, e).

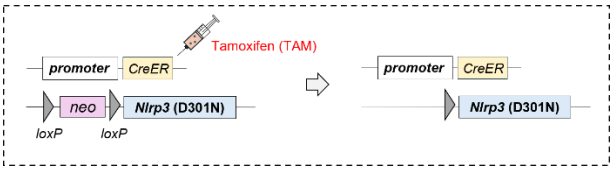

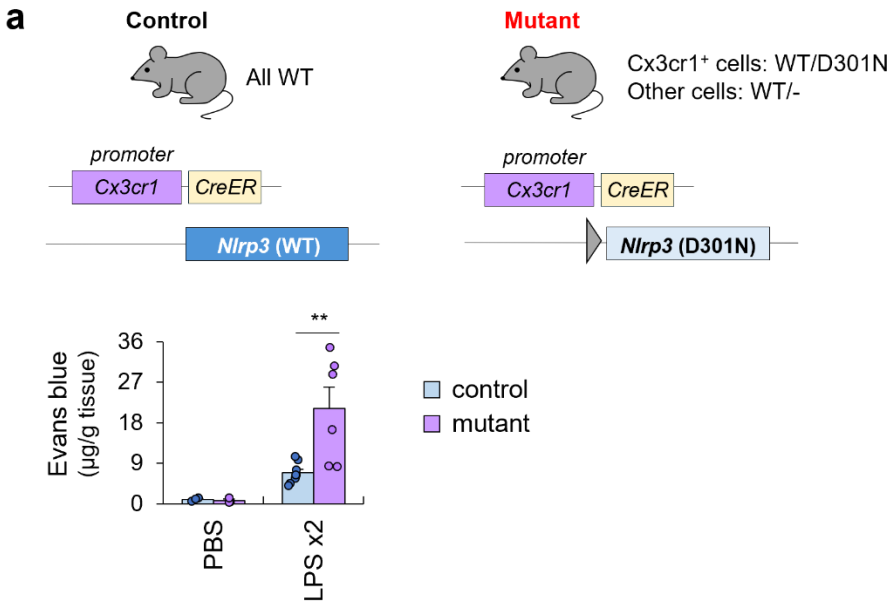

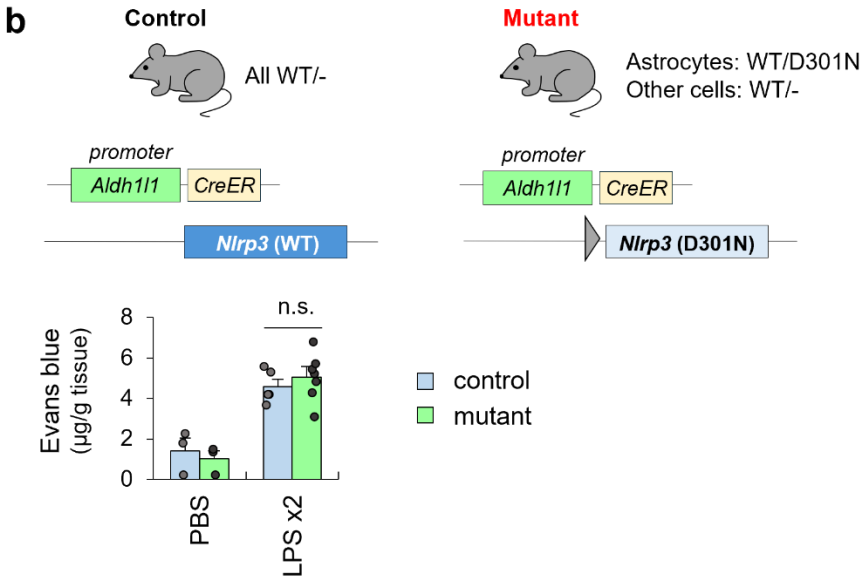

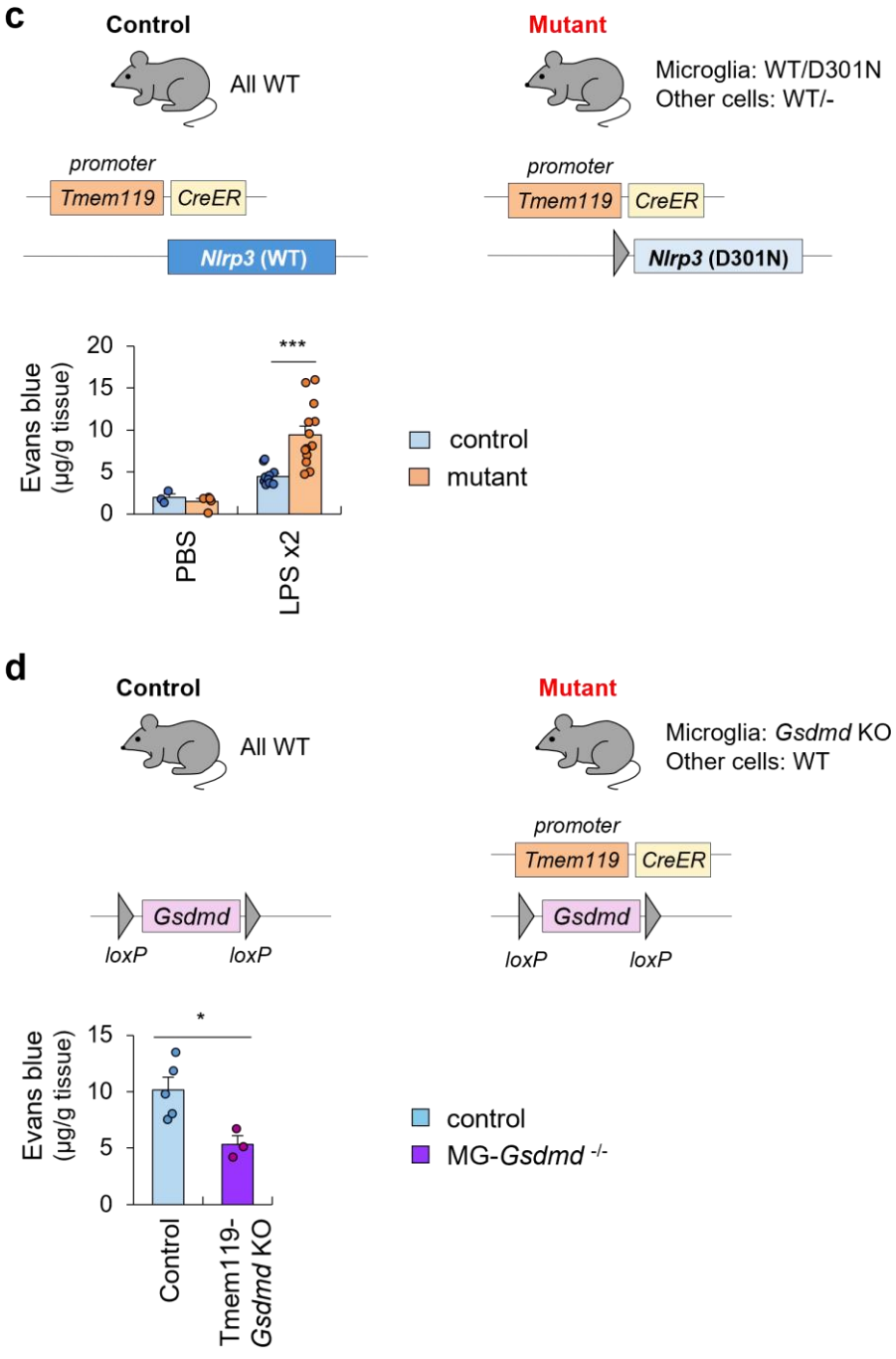

Fig 18. Microglial NLRP3 inflammasome activation is critical in peripherally induced BBB disruption. (a) Explanations on NLRP3 levels in Cx3cr1$^+$ cells and non-Cx3cr1$^+$ cells from control and D301N mutant mice after tamoxifen administration. In mutant mice, D301N mutant form is expressed exclusively in Cx3cr1$^+$ cells (microglia and peripheral myeloid cells). Control and mutant mice administered two intraperitoneal injections of LPS (0.8 mg/kg) in 24 h intervals, and brain tissues were collected 6 h post last injection for Evans blue assay. (n= 3 (PBS), 8 (cont LPS x2), 6 (mut LPS x2)). (b) Explanations on NLRP3 levels in Aldh1l1$^+$ cells and non-Aldh1l1$^+$ cells from control and D301N mutant mice after tamoxifen administration. In mutant mice, D301N mutant form is expressed exclusively in Aldh1l1$^+$ cells (astrocytes). Control and mutant mice administered two intraperitoneal injections of LPS (0.8 mg/kg) in 24 h intervals, and brain tissues were collected 6 h post last injection for Evans blue assay. (n= 3 (PBS), 5 (cont LPS x2), 7 (mut LPS x2)). (c) Explanations on NLRP3 levels in Tmem119$^+$ cells and non-Tmem119$^+$ cells from control and D301N mutant mice after tamoxifen administration. In mutant mice, D301N mutant form is expressed exclusively in Tmem119$^+$ cells (microglia). Control and mutant mice administered two intraperitoneal injections of LPS (0.8 mg/kg) in 24 h intervals, and brain tissues were collected 6 h post last injection for Evans blue assay. (n= 3 (cont PBS), 11 (cont LPS x2), 5 (mut PBS), 13 (mut LPS x2)). (d) Explanations on GSDMD expressions in microglia and other cell types of control and microglial-specific *Gsdmd* knockout mouse after tamoxifen treatment. Control and mutant mice administered two intraperitoneal injections of LPS (0.8 mg/kg) in 24 h intervals, and brain tissues were collected 6 h after last injection for Evans blue assay. (n = 5 (Control), 3 (mutant)). Differences among groups were performed through two-way ANOVA, subsequently analyzed using Bonferroni multiple comparisons test or a two-tailed t-test assuming unequal group pairing, asterisk used to denote statistically significant differences. Results are shown as means ± SEM (a, b, c) (d). **P*< 0.05, ***P*< 0.01, ****P*< 0.001, n.s. not significant.

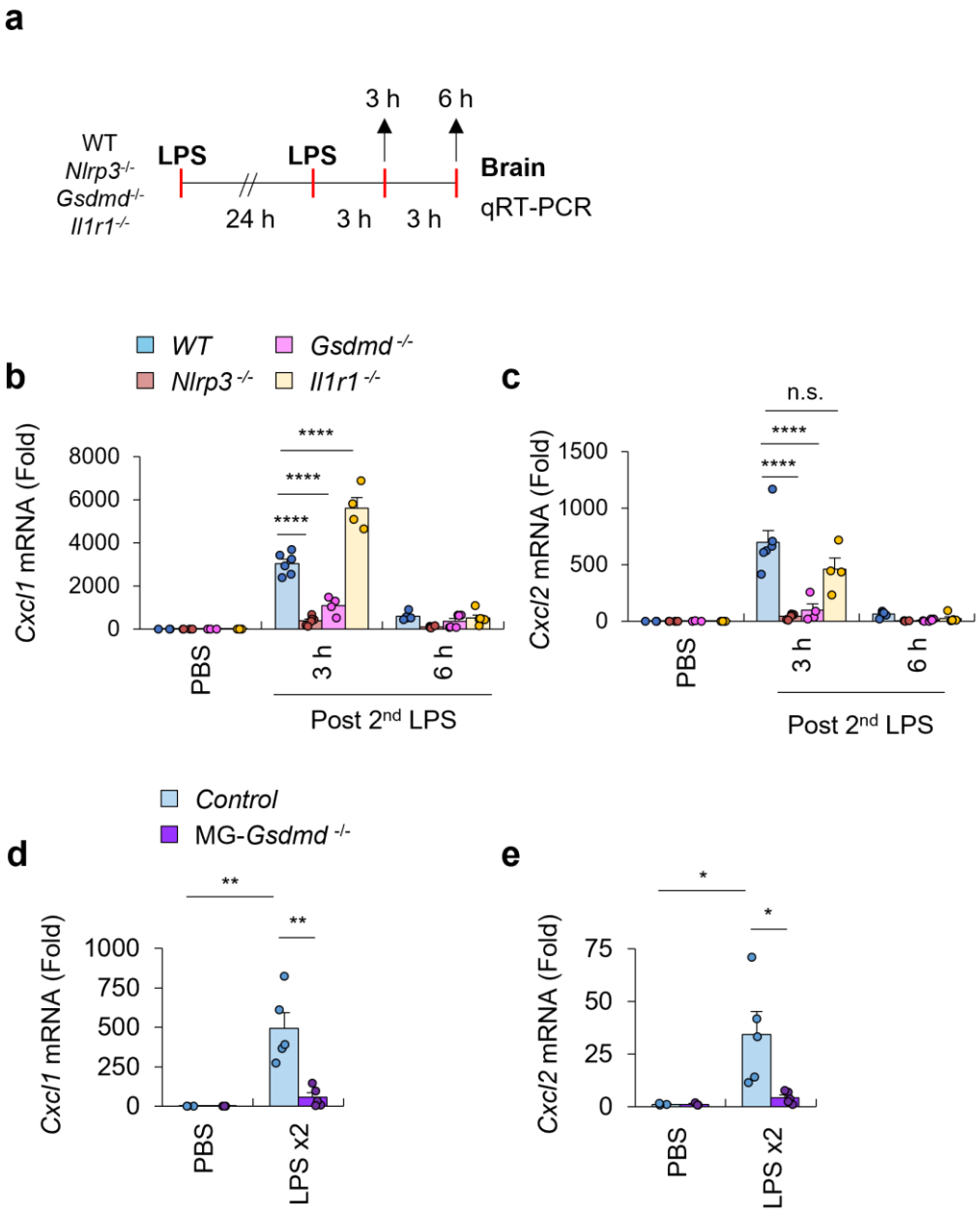

Fig 19. NLRP3-gasdermin D axis mediates chemokine expressions in the brain following peripheral inflammation in an IL-1R signaling-independent manner. (a) Schematic of the experimental design to assess comparative mRNA levels in the brain following peripheral LPS stimulation of WT, *Nlrp3*$^{-/-}$, *Gsdmd*$^{-/-}$, and *Il1r1*$^{-/-}$ mice. Mice administered two intraperitoneal injections of LPS (0.8 mg/kg) in a 24 h interval. Brain tissues were collected at 3 h and 6 h after the final LPS injection. (b, c) Quantitative measurement of comparative *Cxcl1* (b) and *Cxcl2* (c) mRNA expression following repeated LPS administrations as described in (a) using qRT-PCR. (b & c, n = 3 (WT PBS), 6 (WT 3 h), 5 (WT 6h), 4 (*Nlrp3*$^{-/-}$, PBS, 6 h), 6 (*Nlrp3*$^{-/-}$, 3 h), 3 (*Gsdmd*$^{-/-}$, PBS) 4 (*Gsdmd*$^{-/-}$, 3 h), 6 (*Gsdmd*$^{-/-}$, 6h), 4 (*Il1r1*$^{-/-}$, PBS, 3 h), 6 (*Il1r1*$^{-/-}$, 6h)). (d, e) Quantitative measurement of comparative *Cxcl1* (d) *and Cxcl2* (e) mRNA levels in the brain following repeated LPS injections in control and microglia-specific *Gsdmd* deficient mice. (6 h post last LPS treatment). (d & e, n = 3 (PBS), 5 (LPS x2)). Differences among groups were performed through two-way ANOVA, subsequently analyzed using Bonferroni multiple comparisons test, asterisk used to denote statistically significant differences. Results are shown as means ± SEM (b, c, d, e). **P*< 0.05, ***P*< 0.01, *****P*< 0.0001, n.s. not significant.

3.7. Microglial NLRP3-gasdermin D-derived GDF-15 leads to chemokine productions in brain

We hypothesized that certain molecules released through the microglial NLRP3-GSDMD axis may contribute to BBB disruption. To identify the molecules released through the microglial GSDMD pores, we conducted mass spectrometry-based proteomic analysis on the primary cultured microglia isolated from WT and *Gsdmd*$^{-/-}$ mice (Fig. 20 a). Microglia were treated with LPS and ATP to induce the NLRP3 inflammasome activation *in vitro*, and the resulting supernatants were collected and subjected to the proteomic analysis. We first filtered out proteins that were upregulated independently of inflammasome activation, defined as those showing an increase of more than 1.3 times higher in the ATP-only condition relative to PBS controls. Then, by comparing LPS+ATP groups of WT and *Gsdmd*$^{-/-}$ microglia, we identified top 11 candidate proteins that are secreted via NLRP3-GSDMD axis in microglia (Fig. 20 b).

Among these proteins, GDF15 has been implicated in various brain disorders, including Alzheimer's diseases, ischemic stroke, or Parkinson's disease, and it is recognized as a molecule that exacerbates cognitive dysfunction by promoting brain inflammation[72]. Likewise, we observed an upregulation of *Gdf-15* mRNA expression and its protein level in the brain upon repeated LPS injection, while these effects were abrogated in both *Nlrp3*$^{-/-}$ and *Gsdmd*$^{-/-}$ mice (Fig 21 a-c).

To further validate the involvement of GDF-15 *in vivo*, we intravenously injected the recombinant GDF-15 in WT mice (Fig. 22 a). We observed a significant elevation in the *Cxcl* chemokine productions in brain tissue, which implies that GDF-15 induces upregulation of neutrophil-recruiting chemokine expressions in the brain (Fig. 22 b, c). To confirm this, we treated primary mixed glial culture with recombinant GDF-15 *in vitro* (Fig. 22 d). We observed the significant upregulation in *Cxcl* chemokines and *Ccl2* expressions upon GDF-15 treatment, suggesting the potential role of GDF-15 in driving immune cell recruitment into the brain (Fig. 22 e). Collectively, we observed chemokine mRNA levels in brain at 3 hours post LPS injection, a time point when GDF-15 is released upon NLRP3 inflammasome activation, and this elevation in chemokine expressions was highly NLRP3-GSDMD axis-dependent and IL-1β-independent.

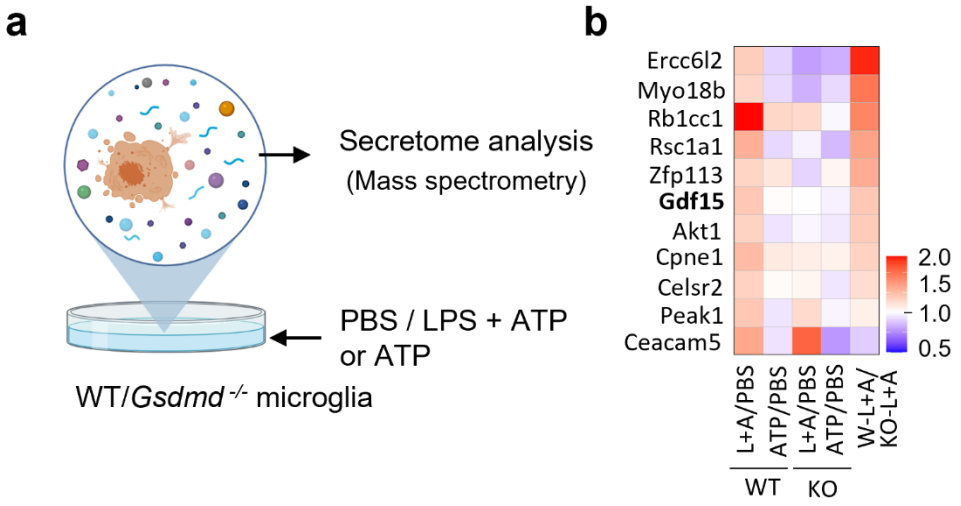

Fig 20. Microglial NLRP3-gasdermin D axis-derived molecules contribute to peripheral inflammation-induced BBB disruption. (a) Experimental scheme of mass spectrometry-based secretome analysis isolated from WT and *Gsdmd*$^{-/-}$ microglia culture treated either with LPS at 0.25 μg/ml for 3 hours followed by ATP at 2.5 mM for 20 min or ATP treatment alone. (b) Heatmap showing the relative levels of leading candidate proteins measured in the culture supernatants collected as described in (a). "L+A" denotes "LPS + ATP". Color intensity indicates a relative abundance of candidate proteins.

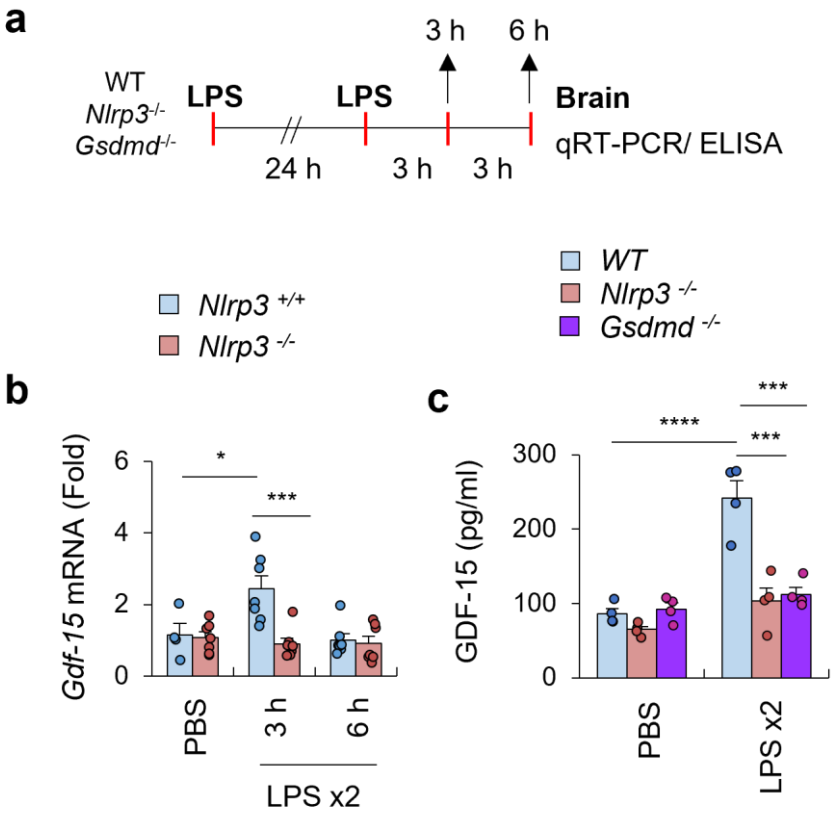

Fig 21. GDF-15 production in the brain following peripheral inflammation is NLRP3-gasdermin D-dependent. (a) Scheme of the experimental design to assess GDF-15 levels in the brain following peripheral LPS stimulation of WT, *Nlrp3*$^{-/-}$, and *Gsdmd*$^{-/-}$ mice. Mice administered two intraperitoneal injections of LPS (0.8 mg/kg) in a 24 h interval. Brain tissues were isolated at 3 h or 6 h after the final LPS challenge. (b) Quantification of relative mRNA levels of *Gdf15* in brain tissues of WT and *Nlrp3*$^{-/-}$ mice 3 and 6 hours after repeated LPS injections as described in (a) using qRT-PCR. (n = 4 (WT PBS), 7 (all the other groups)). (c) Quantitative measurement of protein expressions of GDF-15 in brain tissues of WT, *Nlrp3*$^{-/-}$, and *Gsdmd*$^{-/-}$ mice 3 hours after repeated LPS injections (n = 4 per group) as described in (a) using ELISA. Differences among groups were performed through two-way ANOVA, subsequently analyzed using Bonferroni multiple comparisons test, asterisk used to denote statistically significant differences. Results are shown as means ± SEM (b, c). *P< 0.05, ***P< 0.001, ****P< 0.0001, n.s. not significant.

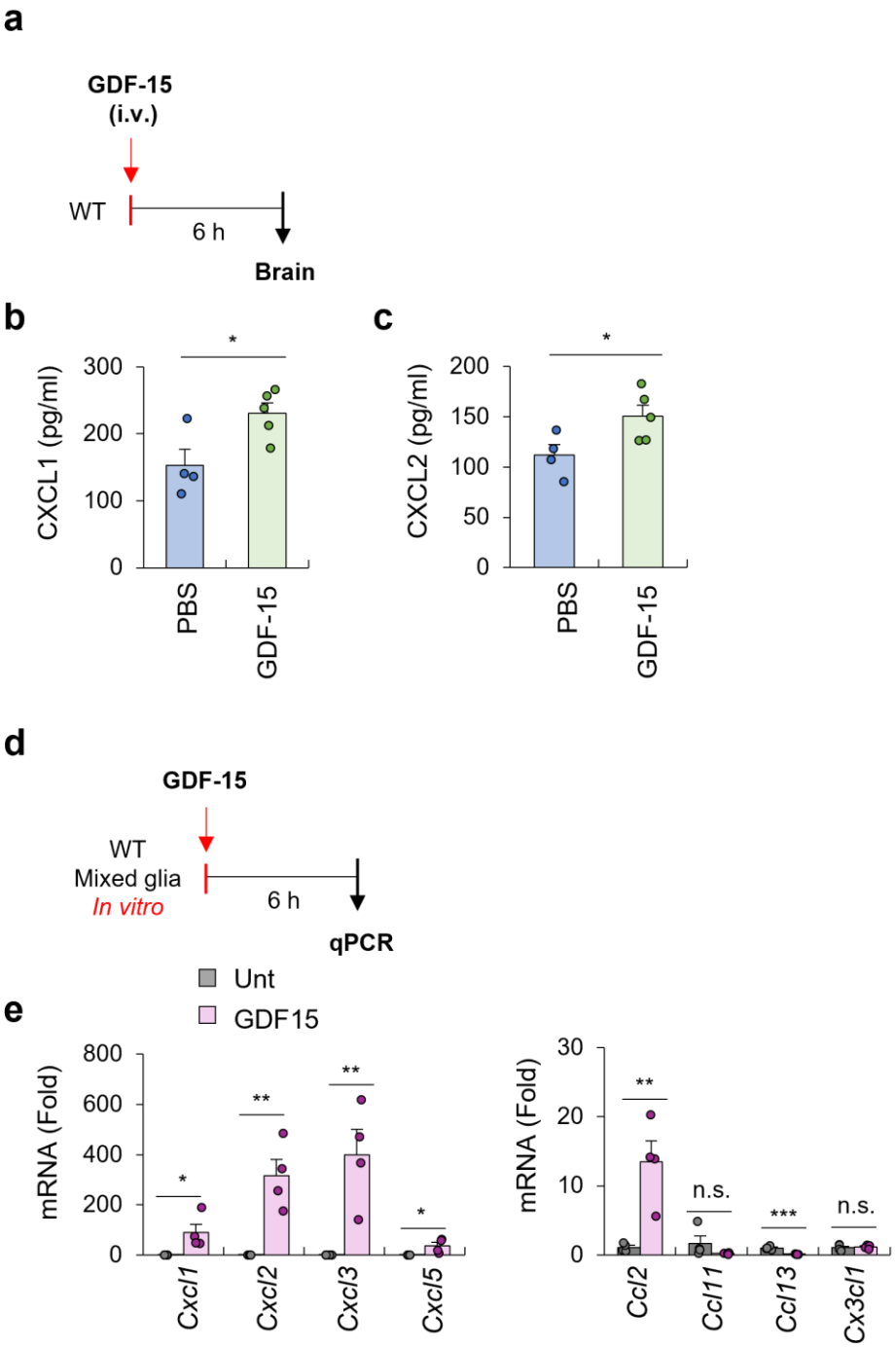

Fig 22. GDF-15 treatment leads to CXCL chemokine expressions in the brain. (a) Experimental scheme of GDF-15 administration in mice. Mice administered an intravenous injection of recombinant GDF-15 (2 μg/ mouse), and brain tissues were collected at 6 h post injection for protein level quantification. (b, c) Quantitative measurement of CXCL1 (b) and CXCL2 (c) protein expression levels in brain tissue lysates as described in (a) using ELISA. (n = 4 (PBS), 5 (GDF15)). (d) Experimental scheme of *in vitro* GDF-15 treatment in primary mixed glial cell cultures at a dose of 100 ng/ml. Cells were harvested for quantification of relative mRNA levels 6 h after GDF-15 treatment. (e) Quantification of various CXCL (*Cxcl1*, *Cxcl2*, *Cxcl3*, and *Cxcl5*) and CCL (*Ccl2*, *Ccl11*, *Ccl13*, and *Cx3cl1*) chemokines mRNA levels in primary mixed glial cells as described in (d). (n = 4 per group). "Unt" denotes "untreated." Differences among groups were performed through a two-tailed t-test assuming unequal group pairing, asterisk used to denote statistically significant differences. Results are shown as means ± SEM (b, c, e). **P*< 0.05, ***P*< 0.01, ****P*< 0.001, n.s. not significant.

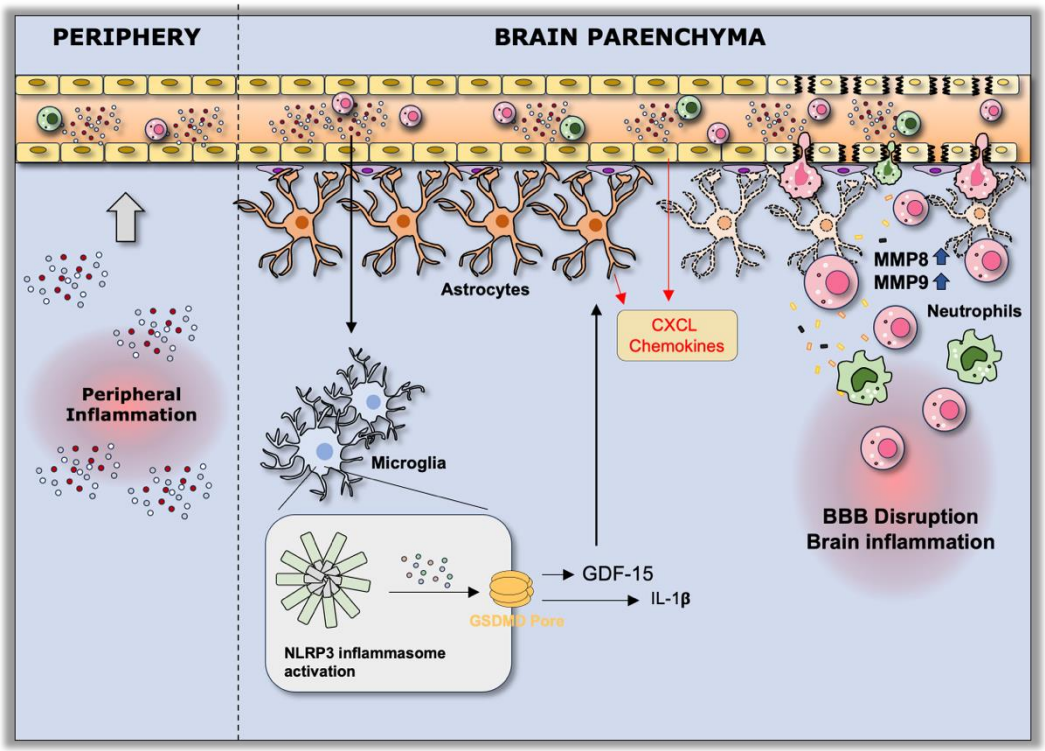

Fig 23. Summary illustrations on proposed mechanism underlying the central role of microglial NLRP3-gasdermin D axis in peripheral inflammation-induced BBB disruption. (a) Peripheral inflammation leads to robust proinflammatory cytokines in blood circulations. (b) Microglial NLRP3 inflammasome is activated in response to peripheral inflammation, which in turn leads to microglial GSDMD pore formations. (c) Microglial NLRP3-GSDMD axis-derived GDF-15 induces generations of CXCL chemokines (CXCL1 and CXCL2) in the brain. (d) These chemokine productions further recruit neutrophils into the brain parenchyma. (e) Neutrophils-derived MMP molecules (MMP8 and MMP9) promotes the disruption of BBB. (f) Microglial NLRP3 inflammasome activation and subsequent neutrophils infiltrations exacerbate neuroinflammation and immune cell infiltrations.

4. DISCUSSION

Previous studies have reported that maintenance of BBB integrity plays crucial roles in mediating neuroinflammation and neurological disorders[12-14]. Therefore, elucidating the cellular mechanisms governing BBB permeability can effectively prevent the disease progression and thus contribute to its treatment. While cumulative studies have highlighted the importance of preserving BBB integrity in the context of neuroinflammatory and neurodegenerative conditions, the precise mechanisms through which peripheral inflammation compromises the BBB remained elusive. This study provides new insight into this process by identifying a microglia-specific signaling pathway that mediates peripheral inflammation-induced BBB disruption independently of classical cytokines. Importantly, the identification of GDF-15 driven chemokine production and neutrophil chemotaxis as key contributors to BBB breakdown reveals potential therapeutic targets. By intervening in this microglia-mediated cascade, it may be possible to prevent the neurovascular changes that precede or exacerbate neurological disease progression, thereby offering a new approach for treatment of inflammatory CNS disorders.

Previous reports have relied on *in vitro* experiments using only endothelial cells, which have limitations in understanding the complex interactions of the BBB-comprising cell types. To address these limitations and understand the cellular processes that control BBB integrity, we aimed to elucidate BBB disruption through direct analysis of changes in brain-resident glial and infiltrating immune cells. We confirmed that one modest dose of LPS is insufficient to trigger detectable changes in the brain microenvironment. Although peripheral inflammatory markers were substantially elevated in the blood, multiple assays consistently demonstrated that brain remained unaffected. Both Evans blue and sodium fluorescein assays showed that BBB permeability remained unaffected under LPS x1 treatment conditions (Fig. 1). Additionally, ELISA and western blot analyses revealed that brain cytokine levels were comparable to those observed in PBS-treated controls (Fig. 2). Consistent with these findings, flow cytometry analysis indicated no increase in immune cell infiltration into brain parenchyma upon single LPS treatment (LPS x1) (Fig 3). A recent study investigating endothelial GSDMD-mediated BBB disruption provides important insights into the mechanisms by which peripheral inflammation compromises BBB integrity. While it emphasizes inflammasome activation under lethal conditions, our work particularly aims to explore the involvement of inflammasome in relatively moderate, non-lethal inflammatory contexts,

conditions that may better reflect the physiological settings relevant to many neurological disorders. In non-lethal conditions, where endothelial cells are supported by surrounding astrocytes and pericytes, we hypothesize that microglia are more readily activated than endothelial cells in response to peripheral immune challenges. Supporting this, the scRNA-seq data reveal that microglia respond to LPS stimulus at levels comparable to endothelial cells, underscoring the importance of microglia as early responders to peripheral inflammatory signals and potential mediators of BBB dysfunction. Collectively, these findings indicate that the cells comprising the BBB serve as an effective first-line defense, preserving the central nervous system integrity in response to acute peripheral inflammatory stimuli.

Although IL-1β and IL-18 have been widely recognized as key mediators of neuroinflammation and neurotoxicity following inflammasome activation, our findings suggest that microglial NLRP3 inflammasome activation induces BBB disruption in an IL-1β-independent manner. Instead, we identified GDF-15 as a novel secretory factor released via the microglial NLRP3-GSDMD axis in response to peripheral inflammation. Corroborating these findings, we observed a robust increase in GDF-15 levels in the brain as early as 3 hours following repeated LPS injection, which is highlyNLRP3 activation-dependent. This early upregulation of GDF-15 preceded and likely contributed to the production of CXCL chemokines, thereby facilitating neutrophil recruitment. Our study highlights GDF-15 as a previously unrecognized effector downstream of microglial inflammasome activation that plays a critical role in mediating BBB disruption. Previous studies have firmly established IL-1β as a key pro-inflammatory cytokine in disease pathogenesis, with its dysregulated expression contributing to tissue damage and inflammation across multiple conditions[73-75]. The therapeutic efficacy of IL-1 receptor antagonists, such as anakinra, has been demonstrated in various inflammatory diseases including rheumatoid arthritis, cryopyrin-associated periodic syndromes, and recurrent pericarditis[76-78]. These findings underscore the central role of IL-1β-mediated inflammation in disease progression and highlight the clinical success of targeting the IL-1 pathway for therapeutic intervention. However, our current study reveals a distinct mechanistic pathway whereby GDF-15, rather than IL-1β, plays a pivotal role in BBB disruption. This GDF-15-mediated BBB disruption mechanism occurs independently of IL-1β, as IL-1β was not required for NLRP3-GSDMD-mediated barrier dysfunction. Given that GDF-15 has emerged as a promising therapeutic target with neutralizing antibodies showing clinical efficacy in cancer immunotherapy and cachexia treatment, GDF-15 inhibition represents a novel and potentially effective therapeutic

approach for neurological conditions that involve BBB disruption.

Within the central nervous system, GDF-15 plays crucial neuroprotective and homeostatic roles. GDF-15 promotes neuronal survival and differentiation during embryonic neuronal development and regulates adult hippocampal neurogenesis by promoting neural stem cell proliferation and migration. Additionally, GDF-15 has been implicated in enhancing synaptic transmission and modulating neural circuits involved in functions such as appetite regulation. Given its broad involvement in maintaining neuronal health and function, systemic inhibition of GDF-15 could lead to adverse effects by disrupting homeostatic processes essential for neuronal development and maintenance. Therefore, a more nuanced understanding of context-specific roles of GDF-15 is essential for developing therapies targeting GDF-15.

It has long been proposed that circulating pro-inflammatory cytokines like IL-1β, IL-6, and TNFα compromise BBB integrity by directly targeting endothelial cells. This effect is thought to occur primarily through the downregulation of cell-cell junction components and adhesion molecules, as demonstrated in various in vitro models. This is mainly attributed to the anatomical localization of endothelial cells, which are in direct contact with blood-borne inflammatory mediators within the vascular lumen. However, given the structural complexity and resilience of the BBB *in vivo*, we speculated that cytokines alone may not be sufficient to induce significant barrier disruption. To prove this hypothesis, we intravenously administered a mixture of IL-1β, IL-6, and TNFα - mimicking the cytokine productions observed during peripheral inflammation - to wild-type and *Nlrp3*-deficient mice. While wild-type mice exhibited apparent BBB leakage, *Nlrp3* knockout mice retained intact barrier function in response to cytokine exposure. These findings suggest that circulating cytokines are less likely to directly disrupt the BBB integrity through stimulating endothelial cells but rather act via a mechanism dependent on NLRP3 inflammasome activation. Additional experiments using conditional knockout mice further confirmed that microglial NLRP3 inflammasome is a major driver of mediating BBB disruption under inflammatory conditions. Together, these results challenge the conventional view that cytokine-mediated endothelial injury is the primary cause of BBB disruption and instead underscore the pivotal role of CNS-resident immune responses - particularly microglial NLRP3 activation - as key drivers of BBB impairment.

Although the BBB plays the role of a structural and functional barrier that limits the entry of peripheral substances into the CNS, our findings suggest that BBB disruption is more likely to occur as a consequence of microglial activation rather than direct damage from circulating cytokines or

other blood-mediated molecules. However, the precise mechanisms by which peripheral inflammation leads to microglial NLRP3 inflammasome activation remain unclear. In particular, it is not yet known which specific factors, probably cytokines or endogenous ligands, act as upstream ligands to trigger inflammasome activation in microglia. Given the molecular size and limited half-life of systemically administered LPS, it is unlikely that LPS directly enters the brain parenchyma. Therefore, we speculate that microglial NLRP3 activation in this context is mediated by unidentified signals associated with sterile inflammation. Further studies should focus on identifying the molecular mediators that bridge peripheral inflammation and microglial inflammasome activation. Elucidating these pathways will be helpful for advancing our understanding of the initial events occurrence that cause BBB disruption and for developing the upstream-targeted therapeutic strategies.

Interestingly, we have observed a notable increase in astrocyte numbers in immunohistochemical analyses. While this finding suggests that astrocytes may respond differently to inflammatory stimuli, the functional significance of their proliferation or activation in the context of BBB disruption remains unclear. To explore the potential involvement of astrocytes, we employed a transgenic mouse where NLRP3 D301N mutant form is expressed specifically in astrocytes. However, this manipulation did not result in significant differences in BBB integrity compared to control mice, suggesting that astrocytic NLRP3 is not a major contributor to BBB breakdown. Nevertheless, it remains possible that astrocytes exert other regulatory roles independent of NLRP3 activation, such as modulating the inflammatory responses or participating in BBB repair processes. Further investigation is warranted to delineate the broader functional roles of astrocytes under peripheral inflammatory conditions.

Repeated LPS administration induced a disruption of the BBB that persisted for at least 24 hours after the second injection. This pattern indicates that the inflammatory insult does not lead to chronic BBB impairment. It is plausible that endogenous repair mechanisms are activated following the damage to restore vascular integrity. Further studies will be required to identify the specific cellular and molecular processes involved in this recovery phase.

While our findings strongly suggest that neutrophil-derived MMPs play a pivotal role in BBB disruption following peripheral inflammation, several limitations remain in directly validating this mechanism. Although we observed active infiltration and perivascular accumulation of neutrophils in the brain using two-photon in vivo imaging after repeated LPS injections, we were unable to

clearly demonstrate their adhesion to the brain vasculature or the localized secretion of MMPs at 3 to 6 hours post LPS injection, the time point when BBB disruption is observed. Moreover, although the MMP inhibitor ilomastat effectively alleviated BBB impairment, it remains uncertain whether this compound sufficiently penetrates the BBB. Therefore, we cannot completely rule out the possibility that MMP inhibition occurred outside the BBB rather than within the brain parenchyma. Importantly, the use of a CXCR2 antagonist, which blocks neutrophil chemotaxis, also significantly rescued BBB integrity, further supporting the critical role of recruited neutrophils in this process. Despite the lack of direct visualization of MMP release, the convergence of evidence from neutrophil depletion, CXCR2 blockade, and MMP inhibition strongly supports our conclusion that neutrophil-derived MMP activity contributes significantly to BBB breakdown. Future studies employing higher-resolution imaging or reporter systems for MMP activity could provide more definitive evidence for this proposed mechanism.

5. CONCLUSION

Peripheral inflammation can affect BBB integrity, yet only little is known about its precise cellular mechanism. While it is previously known that peripheral inflammation affects BBB-comprising cells, our study demonstrated novel roles of microglial NLRP3-GSDMD pathway in BBB disruption triggered by peripheral inflammation and suggested a potential effector mechanism involving molecules generated by NLRP3 activation and their subsequent effects in this process. In brief, Peripheral inflammation results in increased productions of proinflammatory cytokines in the blood. These cytokines and other inflammatory mediators induce microglial NLRP3 inflammasome activation, and we identified GDF-15 to be the key molecules that are released via GSDMD pores, stimulating the productions of CXCL-related chemokines in the brain. The resulting CXCL chemokines act as chemoattractant, guiding circulating neutrophils toward brain blood vessels. Then, neutrophil-derived MMPs trigger the loss in BBB integrity, allowing their infiltration into the brain parenchyma. Infiltrated neutrophils further degrade BBB integrity by releasing MMP8 and MMP9, exacerbating neuroinflammation. Despite our findings on the precise cellular processes underlying peripheral inflammation-induced BBB disruption, we have yet to uncover the specific ligand that activates microglial NLRP3 inflammasome in the brain. Nonetheless, our study clearly demonstrates the pivotal roles of microglia in mediating brain inflammation through the regulation of BBB integrity. These results offer significant implications for understanding a variety of neuropathological conditions, such as Alzheimer's disease, Parkinson's disease, and epileptic seizure, wherein neuroinflammation and BBB dysfunction are central pathophysiological factors. Our study highlights the critical roles of microglia as the primary resident immune cells within the brain and proposes potential therapeutic targets for mitigating neuroinflammation and BBB impairment.

References

1. Xiao M, Xiao ZJ, Yang B, Lan Z, Fang F. Blood-brain barrier: more contributor to disruption of central nervous system homeostasis than victim in neurological disorders. Frontiers in Neuroscience 2020;14:764.
2. Abbott NJ, Rönnbäck L, Hansson E. Astrocyte–endothelial interactions at the blood–brain barrier. Nature reviews neuroscience 2006;7:41-53.
3. Wu D, Chen Q, Chen X, Han F, Chen Z, Wang Y. The blood–brain barrier: Structure, regulation and drug delivery. Signal transduction and targeted therapy 2023;8:217.
4. Stamatovic SM, Keep RF, Andjelkovic AV. Brain endothelial cell-cell junctions: how to "open" the blood brain barrier. Current neuropharmacology 2008;6:179-92.
5. Engelhardt B, Ransohoff RM. Capture, crawl, cross: the T cell code to breach the blood–brain barriers. Trends in immunology 2012;33:579-89.
6. Marchetti L, Engelhardt B. Immune cell trafficking across the blood-brain barrier in the absence and presence of neuroinflammation. Vascular Biology 2020;2:H1-H18.
7. Armulik A, Genové G, Mäe M, Nisancioglu MH, Wallgard E, Niaudet C, et al. Pericytes regulate the blood–brain barrier. Nature 2010;468:557-61.
8. Stebbins MJ, Gastfriend BD, Canfield SG, Lee M-S, Richards D, Faubion MG, et al. Human pluripotent stem cell–derived brain pericyte–like cells induce blood-brain barrier properties. Science advances 2019;5:eaau7375.
9. Ahmad AA, Taboada CB, Gassmann M, Ogunshola OO. Astrocytes and pericytes differentially modulate blood—brain barrier characteristics during development and hypoxic insult. Journal of Cerebral Blood Flow & Metabolism 2011;31:693-705.
10. Kim H, Leng K, Park J, Sorets AG, Kim S, Shostak A, et al. Reactive astrocytes transduce inflammation in a blood-brain barrier model through a TNF-STAT3 signaling axis and secretion of alpha 1-antichymotrypsin. Nature Communications 2022;13:6581.
11. Pociūtė A, Pivoriūnas A, Verkhratsky A. Astrocytes dynamically regulate the blood-brain barrier in the healthy brain. Neural Regeneration Research 2024;19:709-10.
12. Archie SR, Al Shoyaib A, Cucullo L. Blood-brain barrier dysfunction in CNS disorders and putative therapeutic targets: an overview. Pharmaceutics 2021;13:1779.
13. Che J, Sun Y, Deng Y, Zhang J. Blood-brain barrier disruption: a culprit of cognitive decline?

Fluids and Barriers of the CNS 2024;21:63.

14. Knox EG, Aburto MR, Clarke G, Cryan JF, O'Driscoll CM. The blood-brain barrier in aging and neurodegeneration. Molecular psychiatry 2022;27:2659-73.
15. Aryal R, Patabendige A. Blood–brain barrier disruption in atrial fibrillation: a potential contributor to the increased risk of dementia and worsening of stroke outcomes. Advances in Surgical and Medical Specialties 2023:565-97.
16. Gao H-m, Chen H, Cui G-Y, Hu J-X. Damage mechanism and therapy progress of the blood-brain barrier after ischemic stroke. Cell & bioscience 2023;13:196.
17. Ohene Y, Morrey WJ, Powell E, Smethers KF, Luka N, South K, et al. MRI detects blood-brain barrier alterations in a rat model of Alzheimer's disease and lung infection. npj Imaging 2025;3:8.
18. Preis L, Villringer K, Brosseron F, Düzel E, Jessen F, Petzold GC, et al. Assessing blood-brain barrier dysfunction and its association with Alzheimer's pathology, cognitive impairment and neuroinflammation. Alzheimer's Research & Therapy 2024;16:172.
19. Sweeney MD, Sagare AP, Zlokovic BV. Blood–brain barrier breakdown in Alzheimer disease and other neurodegenerative disorders. Nature Reviews Neurology 2018;14:133-50.
20. Kozberg MG, Yi I, Freeze WM, Auger CA, Scherlek AA, Greenberg SM, et al. Blood–brain barrier leakage and perivascular inflammation in cerebral amyloid angiopathy. Brain Communications 2022;4:fcac245.
21. Lau K, Kotzur R, Richter F. Blood–brain barrier alterations and their impact on Parkinson's disease pathogenesis and therapy. Translational neurodegeneration 2024;13:37.
22. Brochard V, Combadière B, Prigent A, Laouar Y, Perrin A, Beray-Berthat V, et al. Infiltration of CD4+ lymphocytes into the brain contributes to neurodegeneration in a mouse model of Parkinson disease. The Journal of clinical investigation 2008;119.
23. Sitovskaya D, Akopyan A, Sokolova T, Zabrodskaya Y. Expression of the Tight Junction Protein Claudin in the Blood-Brain Barrier in the Temporal Lobe of Patients with Drug-Resistant Epilepsy. J, Surgical Case Reports and Images 2024;7:2690-1897.
24. Greene C, Hanley N, Reschke CR, Reddy A, Mäe MA, Connolly R, et al. Microvascular stabilization via blood-brain barrier regulation prevents seizure activity. Nature communications 2022;13:2003.

25. Varatharaj A, Galea I. The blood-brain barrier in systemic inflammation. Brain, behavior, and immunity 2017;60:1-12.
26. Banks WA. The blood-brain barrier in neuroimmunology: tales of separation and assimilation. Brain, behavior, and immunity 2015;44:1-8.
27. Erickson MA, Banks WA. Blood–brain barrier dysfunction as a cause and consequence of Alzheimer's disease. Journal of Cerebral Blood Flow & Metabolism 2013;33:1500-13.
28. Zhang L, Zhou L, Bao L, Liu J, Zhu H, Lv Q, et al. SARS-CoV-2 crosses the blood–brain barrier accompanied with basement membrane disruption without tight junctions alteration. Signal transduction and targeted therapy 2021;6:337.
29. Greene C, Connolly R, Brennan D, Laffan A, O'Keeffe E, Zaporojan L, et al. Blood–brain barrier disruption and sustained systemic inflammation in individuals with long COVID-associated cognitive impairment. Nature neuroscience 2024;27:421-32.
30. Chen Y, Yang W, Chen F, Cui L. COVID-19 and cognitive impairment: neuroinvasive and blood–brain barrier dysfunction. Journal of Neuroinflammation 2022;19:222.
31. Kamintsky L, Beyea SD, Fisk JD, Hashmi JA, Omisade A, Calkin C, et al. Blood-brain barrier leakage in systemic lupus erythematosus is associated with gray matter loss and cognitive impairment. Annals of the rheumatic diseases 2020;79:1580-7.
32. Kikuchi DS, Campos ACP, Qu H, Forrester SJ, Pagano RL, Lassègue B, et al. Poldip2 mediates blood-brain barrier disruption in a model of sepsis-associated encephalopathy. Journal of Neuroinflammation 2019;16:1-12.
33. Jeong H-K, Jou I, Joe E-h. Systemic LPS administration induces brain inflammation but not dopaminergic neuronal death in the substantia nigra. Experimental & molecular medicine 2010;42:823-32.
34. Mapunda JA, Tibar H, Regragui W, Engelhardt B. How does the immune system enter the brain? Frontiers in immunology 2022;13:805657.
35. Sofroniew MV. Astrocyte barriers to neurotoxic inflammation. Nature Reviews Neuroscience 2015;16:249-63.
36. Yamazaki Y, Kanekiyo T. Blood-brain barrier dysfunction and the pathogenesis of Alzheimer's disease. International journal of molecular sciences 2017;18:1965.
37. Xie J, Gorlé N, Vandendriessche C, Van Imschoot G, Van Wonterghem E, Van Cauwenberghe C, et al. Low-grade peripheral inflammation affects brain pathology in the

App NL-GF mouse model of Alzheimer's disease. Acta Neuropathologica Communications 2021;9:1-23.

38. Zhao J, Bi W, Xiao S, Lan X, Cheng X, Zhang J, et al. Neuroinflammation induced by lipopolysaccharide causes cognitive impairment in mice. Scientific reports 2019;9:5790.
39. Bossù P, Cutuli D, Palladino I, Caporali P, Angelucci F, Laricchiuta D, et al. A single intraperitoneal injection of endotoxin in rats induces long-lasting modifications in behavior and brain protein levels of TNF-α and IL-18. Journal of neuroinflammation 2012;9:1-12.
40. Huang X, Hussain B, Chang J. Peripheral inflammation and blood–brain barrier disruption: effects and mechanisms. CNS neuroscience & therapeutics 2021;27:36-47.
41. Galea I. The blood–brain barrier in systemic infection and inflammation. Cellular & molecular immunology 2021;18:2489-501.
42. Gullotta GS, Costantino G, Sortino MA, Spampinato SF. Microglia and the blood–brain barrier: An external player in acute and chronic neuroinflammatory conditions. International Journal of Molecular Sciences 2023;24:9144.
43. Michinaga S, Koyama Y. Dual roles of astrocyte-derived factors in regulation of blood-brain barrier function after brain damage. International journal of molecular sciences 2019;20:571.
44. Brilha S, Ong CW, Weksler B, Romero N, Couraud P-O, Friedland JS. Matrix metalloproteinase-9 activity and a downregulated Hedgehog pathway impair blood-brain barrier function in an in vitro model of CNS tuberculosis. Scientific Reports 2017;7:16031.
45. De Vries HE, Blom-Roosemalen MC, Van Oosten M, De Boer AG, Van Berkel TJ, Breimer DD, et al. The influence of cytokines on the integrity of the blood-brain barrier in vitro. Journal of neuroimmunology 1996;64:37-43.
46. Lopez-Ramirez MA, Fischer R, Torres-Badillo CC, Davies HA, Logan K, Pfizenmaier K, et al. Role of caspases in cytokine-induced barrier breakdown in human brain endothelial cells. The Journal of Immunology 2012;189:3130-9.
47. Gryka-Marton M, Grabowska A, Szukiewicz D. Effect of proinflammatory cytokines on blood-brain barrier integrity. European Cytokine Network 2024;35:38-47.
48. Labus J, Häckel S, Lucka L, Danker K. Interleukin-1β induces an inflammatory response and the breakdown of the endothelial cell layer in an improved human THBMEC-based in vitro blood–brain barrier model. Journal of Neuroscience Methods 2014;228:35-45.

49. TSAO N, HSU H-P, WU C-M, LIU C-C, LEI H-Y. Tumour necrosis factor-α causes an increase in blood-brain barrier permeability during sepsis. Journal of medical microbiology 2001;50:812-21.
50. Haruwaka K, Ikegami A, Tachibana Y, Ohno N, Konishi H, Hashimoto A, et al. Dual microglia effects on blood brain barrier permeability induced by systemic inflammation. Nat Commun 10: 5816. 2019.
51. Li Q, Barres BA. Microglia and macrophages in brain homeostasis and disease. Nature Reviews Immunology 2018;18:225-42.
52. Latz E. The inflammasomes: mechanisms of activation and function. Current opinion in immunology 2010;22:28-33.
53. Fernandes-Alnemri T, Yu J-W, Juliana C, Solorzano L, Kang S, Wu J, et al. The AIM2 inflammasome is critical for innate immunity to Francisella tularensis. Nature immunology 2010;11:385-93.
54. Latz E, Xiao TS, Stutz A. Activation and regulation of the inflammasomes. Nature Reviews Immunology 2013;13:397-411.
55. Urwanisch L, Luciano M, Horejs-Hoeck J. The NLRP3 inflammasome and its role in the pathogenicity of leukemia. International journal of molecular sciences 2021;22:1271.
56. Lamkanfi M, Dixit VM. Inflammasomes and their roles in health and disease. Annual review of cell and developmental biology 2012;28:137-61.
57. Heneka MT, Kummer MP, Stutz A, Delekate A, Schwartz S, Vieira-Saecker A, et al. NLRP3 is activated in Alzheimer's disease and contributes to pathology in APP/PS1 mice. Nature 2013;493:674-8.
58. Obermeier B, Daneman R, Ransohoff RM. Development, maintenance and disruption of the blood-brain barrier. Nature medicine 2013;19:1584-96.
59. Wang J-G, Williams JC, Davis BK, Jacobson K, Doerschuk CM, Ting JP-Y, et al. Monocytic microparticles activate endothelial cells in an IL-1β–dependent manner. Blood, The Journal of the American Society of Hematology 2011;118:2366-74.
60. Yoon S-H, Kim Cy, Lee E, Lee C, Lee K-S, Lee J, et al. Microglial NLRP3-gasdermin D activation impairs blood-brain barrier integrity through interleukin-1β-independent neutrophil chemotaxis upon peripheral inflammation in mice. Nature Communications 2025;16:699.

61. Lee K-S, Yoon S-H, Hwang I, Ma J-H, Yang E, Kim RH, et al. Hyperglycemia enhances brain susceptibility to lipopolysaccharide-induced neuroinflammation via astrocyte reprogramming. Journal of Neuroinflammation 2024;21:137.
62. Wendeln A-C, Degenhardt K, Kaurani L, Gertig M, Ulas T, Jain G, et al. Innate immune memory in the brain shapes neurological disease hallmarks. Nature 2018;556:332-8.
63. Ma J-H, Lee E, Yoon S-H, Min H, Oh JH, Hwang I, et al. Therapeutic effect of NLRP3 inhibition on hearing loss induced by systemic inflammation in a CAPS-associated mouse model. EBioMedicine 2022;82.
64. Kuriakose M, Rama Rao KV, Younger D, Chandra N. Temporal and spatial effects of blast overpressure on blood-brain barrier permeability in traumatic brain injury. Scientific reports 2018;8:8681.
65. Ko YJ, Lee J-W, Yang E-J, Jang N, Park J, Jeon YK, et al. Non-invasive in vivo imaging of caspase-1 activation enables rapid and spatiotemporal detection of acute and chronic inflammatory disorders. Biomaterials 2020;226:119543.
66. Yoon S-H, Hwang I, Lee E, Cho H-J, Ryu JH, Kim T-G, et al. Antimicrobial peptide LL-37 drives rosacea-like skin inflammation in an NLRP3-dependent manner. Journal of Investigative Dermatology 2021;141:2885-94. e5.
67. Wang C, Yang T, Xiao J, Xu C, Alippe Y, Sun K, et al. NLRP3 inflammasome activation triggers gasdermin D–independent inflammation. Science immunology 2021;6:eabj3859.
68. de Almeida LG, Thode H, Eslambolchi Y, Chopra S, Young D, Gill S, et al. Matrix metalloproteinases: from molecular mechanisms to physiology, pathophysiology, and pharmacology. Pharmacological Reviews 2022;74:714-70.
69. Rempe RG, Hartz AM, Soldner EL, Sokola BS, Alluri SR, Abner EL, et al. Matrix metalloproteinase-mediated blood-brain barrier dysfunction in epilepsy. Journal of Neuroscience 2018;38:4301-15.
70. Zhou X, Wu Y, Ye L, Wang Y, Zhang K, Wang L, et al. Aspirin alleviates endothelial gap junction dysfunction through inhibition of NLRP3 inflammasome activation in LPS-induced vascular injury. Acta Pharmaceutica Sinica B 2019;9:711-23.
71. Elliott EI, Sutterwala FS. Initiation and perpetuation of NLRP 3 inflammasome activation and assembly. Immunological reviews 2015;265:35-52.
72. Jiang W-W, Zhang Z-Z, He P-P, Jiang L-P, Chen J-Z, Zhang X-T, et al. Emerging roles of

growth differentiation factor-15 in brain disorders. Experimental and Therapeutic Medicine 2021;22:1270.

73. Aggeletopoulou I, Kalafateli M, Tsounis EP, Triantos C. Exploring the role of IL-1β in inflammatory bowel disease pathogenesis. Frontiers in medicine 2024;11:1307394.
74. Dinarello CA. The IL-1 family and inflammatory diseases. Clinical and experimental rheumatology 2002;20:S1-S13.
75. Dinarello CA. Interleukin-1 in the pathogenesis and treatment of inflammatory diseases. Blood, The Journal of the American Society of Hematology 2011;117:3720-32.
76. Kahlenberg JM. Anti-inflammatory panacea? The expanding therapeutics of interleukin-1 blockade. Current opinion in rheumatology 2016;28:197-203.
77. Dinarello CA, Simon A, Van Der Meer JW. Treating inflammation by blocking interleukin-1 in a broad spectrum of diseases. Nature reviews Drug discovery 2012;11:633-52.
78. Hallegua D, Weisman M. Potential therapeutic uses of interleukin 1 receptor antagonists in human diseases. Annals of the rheumatic diseases 2002;61:960-7.

Abstract in Korean

말초 염증에 의한 뇌혈관장벽 손상기전 규명

뇌혈관장벽은 말초의 독소와 염증으로부터 뇌를 보호하며 뇌 항상성을 유지하는데 중요한 역할을 한다. 뇌혈관장벽의 붕괴는 신경염증을 촉진하여 다양한 신경병리학적 상태를 유발하는 핵심요인이지만, 생리적 조건에서 뇌혈관장벽 붕괴를 조절하는 과정은 아직 명확히 밝혀지지 않았다. 본 연구에서는 말초 염증에 의해 유도되는 뇌혈관장벽 붕괴 과정에서 NLRP3 인플라마좀의 역할을 규명하였다. 반복적인 LPS 투여는 NLRP3 의존적인 뇌혈관장벽 손상을 초래하며, 골수 유래 면역세포의 뇌 침투를 증가시켰다. 세포 특이적 NLRP3 과활성화 마우스 모델을 이용한 실험에서 미세아교세포의 NLRP3 인플라마좀 활성화가 말초 염증에 의한 뇌혈관장벽 붕괴를 악화시키는 주요 인자임을 확인하였다. 마찬가지로 미세아교세포의 가스더민 D (GSDMD) 결손은 LPS에 의한 뇌혈관장벽 손상을 완화시켜, 미세아교세포 NLRP3-GSDMD 축이 뇌혈관장벽 붕괴에 중요한 역할을 한다는 것을 확인하였다. 흥미롭게도, 인터루킨-1β는 NLRP3-GSDMD 매개 뇌혈관장벽 손상에 필수적이지 않았다. 대신, 미세아교세포 NLRP3-GSDMD 축은 GDF-15 분비를 유도하며, 이는 CXCL 케모카인의 발현을 증가시켜 기질금속단백질분해효소 (matrix metalloproteinases)를 발현하는 호중구의 뇌 침윤을 촉진하였다. 본 연구 결과는 미세아교세포 NLRP3에 의해 유도되는 케모카인 생성이 뇌혈관장벽 손상을 유발하는 중요한 기전임을 밝혀내며, 이를 표적으로 한 신경염증 완화 전략의 가능성을 제시한다.

핵심되는 말: 뇌혈관장벽, NLRP3 인플라마좀, 미세아교세포의 NLRP3-GSDMD 축, 말초 염증

PUBLICATION LIST

1. Yoon S-H*, Kim C* et al. Microglial NLRP3-gasdermin D activation impairs blood-brain barrier integrity through interleukin-1β-independent neutrophil chemotaxis upon peripheral inflammation in mice. Nature Communications 2025;16.1: 699.
2. Ma J-H*, Lee E*, Yoon S-H*, Min H* et al. Therapeutic effect of NLRP3 inhibition on hearing loss induced by systemic inflammation in a CAPS-associated mouse model. EBioMedicine 2022;82.
3. Yoon S-H et al. Antimicrobial peptide LL-37 drives rosacea-like skin inflammation in an NLRP3-dependent manner. Journal of Investigative Dermatology 2021;141.12: 2885-2894.